HHS Public Access

Author manuscript

Neurobiol Dis. Author manuscript; available in PMC 2023 February 28.

Published in final edited form as:

Neurobiol Dis. 2023 January ; 176: 105943. doi:10.1016/j.nbd.2022.105943.

Wide-field calcium imaging reveals widespread changes in cortical functional connectivity following mild traumatic brain injury in the mouse

Samuel W. Cramer[a,1], **Samuel P. Haley**[b,1], **Laurentiu S. Popa**[b,1], **Russell E. Carter**[b], **Earl Scott**[b], **Evelyn B. Flaherty**[b], **Judith Dominguez**[c], **Justin D. Aronson**[b], **Luke Sabal**[b], **Daniel Surinach**[c], **Clark C. Chen**[a], **Suhasa B. Kodandaramaiah**[c], **Timothy J. Ebner**[b,*]

[a]Department of Neurosurgery, University of Minnesota, Minneapolis, MN 55455, USA

[b]Department of Neuroscience, University of Minnesota, Minneapolis, MN 55455, USA

[c]Department of Mechanical Engineering, University of Minnesota, Minneapolis, MN 55455, USA

Abstract

>2.5 million individuals in the United States suffer mild traumatic brain injuries (mTBI) annually. Mild TBI is characterized by a brief period of altered consciousness, without objective findings of anatomic injury on clinical imaging or physical deficit on examination. Nevertheless, a subset of mTBI patients experience persistent subjective symptoms and repeated mTBI can lead to quantifiable neurological deficits, suggesting that each mTBI alters neurophysiology in a deleterious manner not detected using current clinical methods. To better understand these effects, we performed mesoscopic Ca^{2+} imaging in mice to evaluate how mTBI alters patterns of neuronal interactions across the dorsal cerebral cortex. Spatial Independent Component Analysis (sICA) and Localized semi-Nonnegative Matrix Factorization (LocaNMF) were used to quantify changes in cerebral functional connectivity (FC). Repetitive, mild, controlled cortical impacts induce temporary neuroinflammatory responses, characterized by increased density of microglia exhibiting de-ramified morphology. These temporary neuro-inflammatory changes were not associated with compromised cognitive performance in the Barnes maze or motor function as assessed by rotarod. However, long-term alterations in functional connectivity (FC) were observed. Widespread, bilateral changes in FC occurred immediately following impact and

*Corresponding author at: Department of Neuroscience, University of Minnesota, Lions Research Building, Room 421, 2001 Sixth Street S.E., Minneapolis, MN 55455, USA. ebner001@umn.edu (T.J. Ebner).

[1]Contributed equally to this work.

CRediT authorship contribution statement

Samuel W. Cramer: Conceptualization, Writing – original draft, Funding acquisition. **Samuel P. Haley:** Investigation, Formal analysis, Writing – review & editing, Visualization. **Laurentiu S. Popa:** Formal analysis, Software, Writing – review & editing. **Russell E. Carter:** Conceptualization, Methodology, Formal analysis, Software, Writing – review & editing, Visualization. **Earl Scott:** Writing – review & editing, Investigation. **Evelyn B. Flaherty:** Writing – review & editing, Investigation. **Judith Dominguez:** Methodology. **Justin D. Aronson:** Software. **Luke Sabal:** Investigation. **Daniel Surinach:** Software. **Clark C. Chen:** Conceptualization, Funding acquisition, Writing – review & editing. **Suhasa B. Kodandaramaiah:** Conceptualization, Funding acquisition. **Timothy J. Ebner:** Conceptualization, Funding acquisition, Writing – original draft, Writing – review & editing.

Declaration of Competing Interest

The authors declare no conflicts of interest pertaining to this work.

Supplementary data to this article can be found online at https://doi.org/10.1016/j.nbd.2022.105943.

persisted for up to 7 weeks, the duration of the experiment. Network alterations include decreases in global efficiency, clustering coefficient, and nodal strength, thereby disrupting functional interactions and information flow throughout the dorsal cerebral cortex. A subnetwork analysis shows the largest disruptions in FC were concentrated near the impact site. Therefore, mTBI induces a transient neuroinflammation, without alterations in cognitive or motor behavior, and a reorganized cortical network evidenced by the widespread, chronic alterations in cortical FC.

Keywords

Traumatic brain injury; In vivo optical imaging; Calcium imaging; Network dynamics; Spatial independent component analysis; Functional connectivity

1. Introduction

Mild traumatic brain injury (mTBI), defined as closed head injury resulting in a loss of consciousness or altered consciousness lasting <30 min (Carroll et al., 2004a, 2004b; Kristman et al., 2014) in the absence of any abnormalities (e.g., skull fracture or intracranial hemorrhage) on structural brain imaging (Blennow et al., 2016), constitutes a major public health concern affecting at least 200–300/100,000 people per year (Lefevre-Dognin et al., 2021). Despite the absence of objective imaging and clinical findings, mTBI is sometimes accompanied by symptoms of nausea and vomiting, dizziness, headache, poor concentration, impaired memory, irritability, and emotional lability (Blennow et al., 2016). In addition to the immediate physical, cognitive, and behavioral symptoms, up to 30% of mTBI patients experience a post-concussive syndrome, characterized by CNS dysfunction >3 months after injury (Blennow et al., 2016). These observations suggest that mTBI deleteriously alters neural dynamics in ways undetectable using current clinical methods. Given the prevalence of mTBI, it is imperative to understand the pathophysiological mechanisms of mTBI in the absence of objective findings. However, most animal models of mTBI involves injury that produce neurological deficits and/or morphological damage (Chen et al., 2014; Lagraoui et al., 2012; Marschner et al., 2019; Taib et al., 2017; Xu et al., 2021).

Characterizing the functional connectivity (FC) of spatially distributed and temporally correlated activity in regions throughout the brain as a “connectome” has emerged as a powerful tool for analyzing local and global network activity in the healthy and diseased brain (Biswal et al., 1995; Caeyenberghs et al., 2017; Fornito et al., 2015). Delineating FC after TBI provides an evaluation of injury-induced local and distributed changes, their association with cognitive and motor deficits, as well as neuroplastic changes over time. In moderate to severe TBI patients, both increased and decreased FC have been reported (Caeyenberghs et al., 2017; Li et al., 2019; Palacios et al., 2017; Rigon et al., 2016), with hyper-connectivity the most common finding. In contrast, decreases in FC are common after mTBI (Johnson et al., 2012; Mayer et al., 2011; Zhou et al., 2012). The complexity of the reported network changes after TBI is likely attributable to the heterogeneities in injury severity, distribution of injury (i.e., focal versus diffuse) as well as time from injury (Caeyenberghs et al., 2017). This inherent heterogeneity renders the study of mTBI in human subjects a fundamental challenge (Katz et al., 2015; Levin and Diaz-Arrastia, 2015).

Animal models offer advantages to study mTBI in the ability to precisely manipulate injury severity as well as the frequency and duration of observations after injury. Prior to the development of techniques to assess FC, animal studies of mTBI largely involved injuries that resulted in observable neurological deficits (Petraglia et al., 2014). Moreover, these studies involved short term histological analyses at single, discrete time points after injury (Creed et al., 2011; Spain et al., 2010; Vascak et al., 2018, 2017). Studies of mTBI without associated neurologic injuries that mimic the clinical presentation in humans are limited. Additionally, there are few studies involving multi-time point assessments of FC after mTBI.

With newer Ca^{2+} imaging technologies, multi-time point assessments of FC are now possible (for review see (Cardin et al., 2020; Lin and Schnitzer, 2016; Ren and Komiyama, 2021)). The goal of this study is to improve our fundamental understanding of mTBI using chronic widefield Ca^{2+} optical imaging and network analysis tools to characterize local and global effects of mTBI on cerebral cortical activity through multi-time point assessments in awake Thy1-GCaMP6 mice (Dana et al., 2014). An advantage of the wide-field Ca^{2+} imaging is that it provides a direct measure of neuronal activity in cortical excitatory neurons (Waters, 2020; Yizhar et al., 2011). To mirror mTBI in human subjects, we used a cortical injury protocol characterized by transient changes in neuroinflammation followed by mTBI, without detectable neurologic injury. We document that mTBI without behavioral or structural findings causes persistent changes to cerebral FC, offering insights into the pathophysiology of human mTBI.

2. Material and methods

2.1. Fenestrated See-Shell design and fabrication

Transparent polymer skulls (i.e., See-Shells) were fabricated as described previously (Ghanbari et al., 2019; West et al., 2022). Briefly, See-Shells consist of a transparent polyethylene terephthalate (PET) film (MELINEX 462, Dupont Inc.) bonded to a polymethylmethacrylate frame (PMMA) (RSF2-GPBK-04, Formlabs Inc.). Prior to implantation, a circular fenestration was created in the PET film over the right primary (M1) and secondary (M2) motor cortices to provide access for the controlled cortical impact (CCI) device tip (Fig. 1A).

2.2. In vivo surgical implantation

All animal studies were approved by and conducted in conformity with the Institutional Animal Care and Use Committee of the University of Minnesota. We used Thy1- GCaMP6f mice (#024276, Jackson Laboratories) for Ca^{2+} imaging and C57BL/6 mice (#000664, Jackson Laboratories) for all other aspects. To limit behavioral confounds, Ca^{2+} imaging data and behavioral data were collected on separate cohorts of mice, including both male and female animals. Implantation of the See- Shells and a custom titanium head-plate was performed as described previously (Ghanbari et al., 2019), including anesthesia, analgesia, monitoring, craniectomy, and post-operative care. The See-Shell was aligned to and placed over the craniectomy, providing optical access to a large portion of the dorsal cerebral cortex (Fig. 1A and D).

2.3. Controlled cortical impact procedure

Controlled cortical impact (CCI) is widely used to induce reproducible, graded brain injuries (Xiong et al., 2013). However, the degree of injury and associated hemorrhagic tissue that results from commonly used parameters would interfere with Ca^{2+} optical imaging of brain activity. Also, our goal was to model human mTBI characterized by limited tissue damage and no hemorrhage, with the latter being consistent with the definition of mTBI by the US Department of Veterans Affairs and Department of Defense (Management of Concussion/mTBI Working Group, 2009). Therefore, to minimize damage while imparting a relevant, mild brain injury (Wu et al., 2022; Xu et al., 2021), a modified CCI injury used a rounded 2 mm diameter CCI tip constructed of flexible PMMA (Chen et al., 2014). Prior to the first impact, a single subcutaneous dose of SR buprenorphine (0.2 mg/kg, ZooPharm) was administered, and a dose of meloxicam (2 mg/kg, Bayer Pharmaceutics) before each impact. Using the CCI device (Hatteras Instruments, Model PCI3000), an impact to a 1 mm depth at 0.4 m/s with an 85 ms dwell was delivered perpendicular to the dorsal surface of the brain once per day over 3 days (Fig. 1B and C), as testing showed that faster speeds or a metal tip resulted in hemorrhage and/or structural damage (see Supplementary Fig. 1). The protective silicone seal (Kwik-Sil, World Precision Instruments) overlying the fenestration in the See-Shell was removed and replaced for each impact. The injury was applied to the right M1/M2 motor regions. Sham animals underwent identical procedures without application of the CCI.

2.4. Histology

A subset of 39 mice (n = 18 sham, n = 21 mTBI), 15.0 ± 4.5 weeks old at the time of the first impact, were used for histological analysis. The animals were fully anesthetized in 5% isoflurane and transcardially perfused with phosphate-buffered saline (PBS) followed by 4% paraformaldehyde (PFA). Brains were extracted and fixed in 4% PFA at 4 °C for one week. Two days prior to slicing, the brains were transferred to 30% sucrose solution for dehydration. Coronal slices were cut at 50 μm and kept in PBS solution containing Triton X-100 and blocking agent (Normal Serum Block, CAT# 927502, Biolegend) for 2 h after which they were incubated in a solution containing: 1:1000 primary antibody goat Polyclonal anti-Iba-1 (NB100–1028SS, Novus Biologicals) and rabbit Polyclonal anti-GFAP (PA5–16291, ThermoFisher Scientific) for 24 h at 4 °C. Slices were washed and incubated in solution containing the secondary antibody (1:400) conjugated with fluorophores donkey Polyclonal anti-goat Cy5 (705–175–147, Jackson ImmunoResearch Laboratories); donkey Polyclonal anti-rabbit Alexa Fluor Plus 488 (A32790, ThermoFisher Scientific); donkey Polyclonal anti-mouse Rhodamine Red-X (715–295–150, Jackson ImmunoResearch Laboratories). Slices were then washed in PBS and mounted using Invitrogen ProLong Diamond Antifade Mountant with DAPI (P36962, Invitrogen, ThermoFisher).

2.5. Epifluorescence imaging acquisition and quantification of GFAP and Iba-1 immunofluorescence

Brain sections immunostained for GFAP and Iba-1 were imaged with a Leica DM6000B epifluorescence microscope with a 20× (0.5 NA) objective and tiled using Leica LAS X software. Bilateral regions of interest (ROIs) were outlined on each brain slice image

(Schindelin et al., 2012). Using ImageJ (NIH), Iba-1 expressing cells were counted within each ROI to quantify cell density. For quantifying the GFAP fluorescence, we used a custom ImageJ macro to perform a background subtraction, apply a Gaussian Blur with a radius of 4, and converted to a binary image. Then, an ROI was drawn and the % GFAP expression was quantified by measuring the percentage of pixels with value of 1 in the ROI from the binary image.

2.6. Confocal image acquisition and characterization of microglial morphology

Iba-1 sections were imaged with an Olympus FV1000 scanning laser confocal microscope (40×, 1.3 NA objective) with a 635 nm laser. Confocal stacks were taken at 1024 × 1024 pixels and a step size of 0.57 μm. Images were preprocessed with a custom ImageJ script and quantified with 3Dmorph (York et al., 2018) to determine the ramification index and number of branch points. Images were taken in layers II/III and V/VI in the primary motor cortex. No differences in the microglial morphology were observed between layers, so the results were combined.

2.7. Rotarod

Mice were placed on the rotarod (Ugo Basile Mouse Rota-Rod #47600) with linearly increasing velocity from 5 to 50 RPM, over 3 min. If the mouse spun around twice or fell off during the test, the mouse was removed and the time of failure recorded. The maximum time allowed for was 3 min. Mice were given 3 consecutive training days consisting of 4 trials/day, with a 10-min inter-trial interval. Mice were tested for 3 consecutive days prior to the CCIs, and 3 days after. Rotarod evaluation was performed on 12 mTBI and 13 sham mice that were 14.4 ± 5 weeks old at the time of the first impact.

2.8. Barnes maze

The Barnes maze consisted of a 60 cm diameter circular table with 20 holes (19 false and 1 escape) each with a 5 cm diameter. The false holes were recessed 1 cm into the table. Visual cues were placed on 3 of the surrounding walls. The arena was lit with four 60 W incandescent light bulbs.

During the acquisition phase, mice completed 4 trials/day for 4 consecutive days (Day −5 to −2 relative to CCI, see Fig. 10B). Animals were placed in a cylinder in the center of the dark maze. To begin each trial, the lights were turned on, the cylinder was lifted, and the mice were given 3 min to explore the maze. If the mouse did not enter the escape hole within 3 min, it was manually placed inside the hole for 1 min and then transferred back to its home cage. On each day, the escape hole remained in the same location. The Barnes maze was cleaned with 70% EtOH between trials.

A single probe trial was conducted on Day −1, with the mouse given 90 s to search the maze. The CCI protocol was administered over the next 3 days. The relearning phase was conducted on Days 1 and 2, with the maze rotated 135°, following the same procedure as the acquisition phase. Day 3 consisted of a second probe trial. Barnes maze evaluation was performed on 7 mTBI and 6 sham mice on the 5 days immediately before the first CCI and the 3 days immediately following the final CCI. An additional cohort of 3 mTBI and 3 sham

mice were tested 10 days following the final CCI. Animals used in the Barnes maze task were 12.6 ± 2.1 weeks old at the time of the first impact.

2.9. Barnes maze analysis

Videos of each trial were recorded (BlackFly S USB3, Point Grey) and pose estimation was analyzed with DeepLabCut (Mathis et al., 2018). By labeling the head, center of the body, and base of the tail, a custom MATLAB script tracked pose positions and trajectories to determine the latency to first interaction with the escape hole and number of hole poke errors. Escape latency was defined as the time from when the mouse was released to when the marker on the head initially crossed the escape hole boundary. Poke errors were counted for each instance the point on the head crossed a false hole boundary. Consecutive errors on the same hole were included if the delay was >75 ms between pokes.

2.10. Wide-field Ca^{2+} imaging

Thy1- GCaMP6f mice (n = 4 sham, n = 8 mTBI) were head-fixed on a custom disk treadmill and imaged as detailed previously (West et al., 2022). The animals were 13.7 ± 2.9 weeks old at the time of the first impact. Single-photon fluorescence imaging used a sCMOS camera (Andor Zyla 4.2, Oxford Instruments) controlled with MetaMorph (Molecular Devices Inc.). Dual-wavelength Ca^{2+} imaging interleaved Ca^{2+}-dependent (470 nm) and Ca^{2+}-independent (405 nm) GCaMP6f signals (Cairn OptoLED driver, Cairn OptoLED, P1110/002/000; P1105/405/LED, P1105/470/LED) to mitigate hemodynamic effects and other Ca^{2+}-independent fluorescence changes (Allen et al., 2017; Jacobs et al., 2020; MacDowell and Buschman, 2020; Musall et al., 2019). Exposure times (18 ms) were synchronized via TTL pulses (Cambridge Electronics 140, Cambridge Electronic Design Limited) controlling both LEDs and the camera. Frames (256 × 256 pixels) were captured at 40 Hz (20 Hz/channel).

The field-of-view was optimized to the exposed dorsal cortical surface (38.4 mm^2) with a spatial resolution of 24.2 μm × 24.2 μm/pixel. Calcium imaging data was collected 2 days a week for the 2 weeks prior to the previously described CCI procedure and up to 7 weeks following. Post-CCI imaging began 5 days after the final impact was administered. During an imaging session, 6–10 trials (6000 frames, 5 min) were recorded with a 1–5 min inter-trial interval.

We note that for the Ca^{2+} imaging time points, while not identical to the times used for the behavioral tests, the evaluation times are comparable. Both the Barnes maze and rotarod evaluations were performed 3 days after the last impact. The first imaging session was performed 5 days after the last impact. We also tested an additional cohort in the Barnes maze in which the performance was evaluated 10 days after final impact, comparable to the second week of imaging at ~ day 12 following the final impact.

2.11. Ca^{2+} imaging analysis using spatial Independent Component Analysis (sICA)

Each trial was motion corrected using a subpixel image registration algorithm (Guizar-Sicairos et al., 2008). At the pixel level, both Ca^{2+}-dependent and Ca^{2+}-independent signals were detrended and normalized to the mean fluorescence. Hemodynamic correction was

performed by subtracting the normalized Ca^{2+}-independent signal from the normalized Ca^{2+}-dependent signal, equivalent to published procedures (Jacobs et al., 2020; MacDowell and Buschman, 2020; Ma et al., 2016; West et al., 2022). We acknowledge that there remain differences of opinion on the best method for hemodynamic correction in wide-field Ca^{2+}imaging investigations. As noted above many studies have used dual wavelength, epifluorescence imaging at 405 and 470 nm and a subtraction approach comparable to the present methods (e.g., (Allen et al., 2017; Couto et al., 2021; Jacobs et al., 2020; MacDowell and Buschman, 2020; Musall et al., 2019). Another approach was proposed using dual wavelength imaging based on 530 nm reflection and 470 nm epifluorescence, followed by division of the two signals to remove the hemodynamic contribution (Ma et al., 2016). Therefore, while more accurate hemodynamics correction methods may exist, a recent paper acknowledged that there is presently no agreement on the optimal approach (Couto et al., 2021).

For each mouse, motion corrected data across all sessions were registered to a common frame using a MATLAB affine transform. Then, a binary mask separating the brain from the background was determined for each mouse. Subsequent analysis was restricted to the pixels over the cerebral cortex. After registration, the hemodynamic corrected Ca^{2+} signal was denoised using a linear regression that eliminated the variance associated with the mean time course of all the pixels outside of the mask.

Denoised fluorescence data from all trials were concatenated and compressed to the first 200 components using singular value decomposition (SVD). We computed 60 independent components (ICs) and their time courses using the Joint Approximation Diagonalization of Eigenmatrices (JADE) algorithm that decomposes mixed signals into ICs by minimizing the mutual information with a series of Givens rotations (Cardoso, 1999; Makino et al., 2017; Sahonero-Alvarez, 2017). This method provides a blind source segmentation of the cerebral cortex based only on statistical properties of the Ca^{2+} fluorescence signal. The ICs were z-scored and binarized using a threshold of 2, and ICs covering <400 pixels (~0.23 mm^2) were discarded as physiologically irrelevant. Any IC that included multiple discontinuous regions, for example, homotopic cortical regions, was separated for subsequent analyses. Upon visual inspection, we eliminated ICs that were edge or vascular artifacts (Makino et al., 2017; West et al., 2022).

Functional connectivity of the ICs, corresponding to network nodes, was determined using the adjacency matrices of the Pearson correlations between IC time courses over 1-min, non-overlapping intervals. To quantify the global mTBI effects on FC, we computed the global modularity and global efficiency for each 1-min adjacency matrix (Rubinov and Sporns, 2010). To determine the effect of mTBI, the values were grouped by week post-mTBI and baseline (pooling the two pre- mTBI weeks). The post-mTBI weekly values were compared to the baseline values using an ANOVA with Bonferroni's post-hoc correction ($p < 0.05$, GraphPad Prism GraphPad Software). A Similarity Index was determined using a 2-D Pearson correlation between adjacency matrices. We compared the week prior to mTBI (W-1) to each of the other weeks with an ANOVA with Bonferroni's post-hoc correction ($p < 0.05$, GraphPad Prism GraphPad Software).

We also evaluated the spatial structure of the larger changes in FC due to mTBI. For each pair of ICs, we determined whether the baseline and weekly post-mTBI correlation populations came from different distributions. We used a Kolmogorov-Smirnoff test, with Bonferroni correction to account for all IC pairs, and an effect size threshold that required the difference between baseline mean and each weekly mean to exceed 0.3. The IC pairs that met both criteria, referred to as the Δ networks, describe the extent of the mTBI effect on cortical FC. To quantify changes in the Δ networks across mice, nodes were separated into subnetworks of increased or decreased changes in correlations, and the number of nodes present in each subnetwork was averaged per animal per week and compared between sham and mTBI groups using an ANOVA and a Fisher's exact test with Bonferroni's post-hoc correction ($p < 0.05$) to determine significant changes per week.

2.12. Ca^{2+} imaging analysis using localized semi-nonnegative matrix factorization (LocaNMF)

To provide additional insights into cortical alterations following mTBI, we performed an alternative analysis using LocaNMF (Saxena et al., 2020), a form of multinomial principal component analysis. While sICA has many advantages to assess changes in FC (Calhoun and de Lacy, 2017), averaging across animals is challenging, as the number and position of the ICs varies across animals. LocaNMF uses the Allen Brain Atlas Common Cortical Framework (CCF) for anatomical segmentation, facilitating averaging results across animals (Lein et al., 2007).

The masked, aligned, and hemodynamic corrected data was segmented into 1-min, non-overlapping intervals, denoised, and aligned to the CCF. LocaNMF was run on each interval, allowing for 3 spatial components per atlas region, 100 minimum pixels required for a spatial component (as opposed to 400 used in sICA due to the size limitations of some atlas regions), 80% localization threshold, and capturing 99% of the variance in the data. Canonical correlation coefficients were calculated for each atlas region pair to generate the adjacency matrices over all intervals. False discovery rate was used to determine the significance of correlations between regions (Genovese et al., 2002). Only atlas regions visible after masking across all mice were used for subsequent analysis. Global efficiency, nodal strength, and clustering coefficient were calculated on each non-thresholded, weighted adjacency matrices. The distribution of each metric from each week was normalized to the distribution of the baseline period and compared using a 2-way ANOVA with Bonferroni's post-hoc correction ($p < 0.05$).

A total of 23 atlas regions were found in common across all mice. These regions include: MOp: primary motor cortex; MOs: secondary motor cortex; RSP: retrosplenial cortex (agl: lateral agranular part; d: dorsal part); SSp: primary somatosensory cortex (bfd: barrel field; ll: lower limb; tr: trunk; ul: upper limb; un: unassigned); VIS: Visual cortex (al: anterolateral; am: anteromedial; pm: posteromedial; rl: rostrolateral). Left (contralateral to impact) and right (ipsilateral to impact) hemispheres are denoted as _L and _R, respectively.

2.13. Experimental design and statistical analysis

In addition to the FC statistical analyses described above, statistical evaluation of changes in immunofluorescence, microglial morphology, and behavioral measures between mTBI and sham animals were performed using an ANOVA with Bonferroni's post-hoc correction ($p < 0.05$) using MATLAB (The MathWorks) or GraphPad Prism (GraphPad Software). In the text and figures, all values are reported as mean ± SD. When describing the results of an experiment, "n" refers to the number of animals used.

3. Results

3.1. Histological characterization of the mTBI model

Astrogliosis is a hallmark of a brain injury, including TBI (Burda et al., 2016). Therefore, to evaluate the extent of neuroinflammation induced by our protocol, histological evaluation of the astrocytic marker, GFAP, in brain sections from mTBI and sham animals was performed at 24, 48, and 72 h as well as 6 w post-procedure (Fig. 2A and B). A significant increase in GFAP expression was observed at 24 h following mTBI compared to sham in the cortex ipsilateral to the injury ($F(1,107) = 11.88$, $p = 0.0008$). This increase in GFAP expression progressively decreased each day following injury and normalized by 72 h post-mTBI.

Neuroinflammation often correlates with clinical outcomes following TBI (Kumar et al., 2016; Loane et al., 2014; Loane and Kumar, 2016) and activated microglia are a critical element of this response. We examined microglial activation, via immunostaining for Iba-1 and found a significant increase in microglia cell density between mTBI and sham groups in the cortex ipsilateral to the injury ($F(1,107) = 7.195$, $p = 0.00085$, Fig. 2C and D). At subsequent time-points post-injury, the density of Iba-1 expressing cells normalized between mTBI and sham in the ipsilateral cortex. Therefore, the neuroinflammatory response was transient and normalized within 72 h post-mTBI. Finally, we did not observe any injury to subcortical structures such as the hippocampus or striatum suggesting the injury was highly localized to the cortex.

To further characterize microglia activation, we quantified the 3-dimensional (3D) morphology of Iba-1 expressing cells. High-resolution confocal images show less ramified morphology and shorter branch length in microglia following mTBI at 24 and 48 h, characteristic of an activated state (Loane et al., 2014; Loane and Kumar, 2016) (Fig. 2E). Quantification of microglia morphology reveals a significant reduction in ramification 24 h following mTBI compared to sham ($F(1,31) = 4.98$, $p = 0.0330$), with no significant change at later time points (Fig. 2F). Taken together, our mTBI protocol exhibits transient neuroinflammation, in the form of astrogliosis and microglial activation, that subsides within 48–72 h after the injury.

3.2. Ca^{2+} imaging and functional connectivity of the dorsal cerebral cortex based on sICA

As desired, the parameters used for the CCI produced histological changes, while retaining optical access for wide-field Ca^{2+} imaging of cortical neuronal dynamics. Weekly imaging sessions were performed (sham = 4, mTBI = 8) for 2 weeks prior to mTBI, followed by either 4 weeks (sham =1 and mTBI = 4) or 7 weeks after mTBI (sham = 3 and mTBI =

4) (see Fig. 1C). Mice were head-fixed over a disk treadmill that allowed for spontaneous locomotion and wide-field Ca^{2+} imaging performed through the implanted polymer optical window (see Material and methods). After preprocessing and hemodynamic correction, each cortical surface was functionally segmented using sICA of the entire data set, including both pre- and post-mTBI recordings (420,000 to 650,000 frames per mouse). This resulted in a set of ICs and their associated time courses for each mouse that were used for the subsequent functional analyses.

The sICA segmentation of the dorsal cerebral cortex resulted in 18–22 ICs per mouse, consistent with previous reports (Makino et al., 2017; West et al., 2022). The ICs provide a functional segmentation encompassing the majority of the dorsal cerebral cortex in the imaging field for both sham and mTBI mice (Fig. 3A and B, respectively). Neither the number of ICs ($t(10) = 1.45$, $p = 0.1776$) nor the average coverage achieved ($t(10) = 0.51$, $p = 0.6183$) differed in the two groups (Fig. 3C and D). In the upper right quadrant, near the fenestration and impact site, ICs were identified in the mTBI mice as well as the sham, showing that the Ca^{2+} signals near the fenestration were not disrupted. While there are similarities in the ICs, the exact location and size of the ICs differs for each mouse, as observed previously (West et al., 2022).

The FC was determined for each week, pre- and post-mTBI. The Pearson correlations between all pairs of IC time courses, restricted to the week of interest, were used to generate the FC adjacency matrix for each mouse. Supplementary Fig. 2 provides examples of the Ca^{2+} fluorescence time courses for a small number of ICs in a sham and mTBI mouse and the changes in the Pearson correlation among those ICs compared to baseline over time. The FC network was plotted on an outline of the cortex, with the centers of mass for each IC as the network node coordinates and the edges as the strength of correlation, ρ, between nodes (only edges with $\rho \geq 0.3$ are shown, Fig. 4A and B). As shown for an example sham mouse, the network is qualitatively stable over 9 weeks (Fig. 4A). Qualitative assessment from an example mTBI mouse shows a decrease in FC post-mTBI (Fig. 4B). This qualitative assessment is confirmed by examining the average correlation strength for all connections, normalized to the average baseline strength (Fig. 4C). This measure of normalized network strength significantly decreases for weeks 1–5 following mTBI ($F(7, 3449) = 52.99$, $p < 0.0001$). Correlation strength for the sham group did not decrease but increased at weeks 4 and 5 ($F(7, 1909) = 3.195$, $p = 0.0023$). The decrease in correlation strength suggests that mTBI reduces the overall FC of the dorsal cerebral cortex.

In addition to normalized network strength, we evaluated several other measures of the global network topology following mTBI. To quantify the stability of the IC-based network, we calculated a Similarity Index (see Material and methods), comparing the week prior to mTBI (W-1) with each of the other weeks. For the sham group, the Similarity Index is above 0.75 for all comparisons and there are no significant differences across weeks ($F(7, 21) = 0.97$, $p = 0.48$, Fig. 5A). In contrast, mTBI induces changes in the network structure, resulting in significant decreases of the Similarity Index for weeks 1 through 7 ($F(7, 44) = 5.94$, $p < 0.0001$, Fig. 5A). Analysis of the full network shows that global modularity in the sham group presents no significant changes relative to baseline ($F(7,1909) = 1.819$, $p = 0.0795$, Fig. 5B), while the mTBI group presents significant increases in weeks 1 to

6 ($F(7,3449) = 22.00$, $p < 0.0001$, Fig. 5B). The global efficiency of the full network in the sham group presents an increase in weeks 5 and 6 ($F(7,1909) = 10.66$, $p < 0.0001$, Fig. 5C) relative to baseline, as opposed to decreases in weeks 1 to 6 for the mTBI group ($F(7,3449) = 127.5$, $p < 0.0001$, Fig. 5C). Together, the decreased Similarity Index and increase modularity following mTBI indicate the network is more divided, and the decreased global efficiency is consistent with a reduced ability to integrate neural activity through the network.

Concerning the significant increase in global efficiency at weeks 4–5 in the sham cohort, this increase contrasts with the decrease in global efficiency found in the mTBI group at weeks 1–6. The increase in global efficiency is transient, as opposed to the more persistent changes in FC found in the mTBI mice. Finally, the increase in global efficiency in the sham cohort is isolated to this single measure. In several other FC network measures, including the Similarity Index and modularity (Fig. 5A and C), there were no significant changes in the sham cohort. Therefore, the increase in global efficiency in weeks 4–5 likely represents the natural variability in this FC measure.

The complete networks are complex as are the differences in the global network metrics, so to better understand the larger FC changes, we determined the networks that include only the node pairs with the largest significant changes in correlation (Δ networks, see Material and methods). To determine the significant changes in correlations we computed the FC over 1-min non-overlapping intervals for each week and compared each node pair's weekly correlation population to a baseline population that combined the 2 weeks before mTBI (see Material and methods). In addition to a Bonferroni corrected Kolmogotov-Smirnoff test to determine the significant differences between baseline and the post-mTBI/sham groups, we also required that the absolute difference between the mean correlations exceed 0.3. Examples from the sham group reveal remarkably sparse Δ networks (Fig. 6A), with only a small number of nodes and edges differing from baseline. For mice in the mTBI group, the Δ networks are extensive, covering large expanses of the cortical area. Many nodes and edges change relative to baseline, with the changes dominated by decreases in correlation strength (Fig. 6B). The connectivity changes are not restricted to the cortical impact site in the right M1/M2 motor cortices. Instead, network changes are present throughout the dorsal cerebral cortex, both ipsilateral and contralateral to the site of impact, and the changes persist for up to 7 weeks following mTBI.

To quantify the Δ networks, they were separated into subnetworks of increased or decreased correlations. There are a larger number of nodes with decreased ($F(1, 55) = 42.64$, $p < 0.0001$) and increased ($F(1,55) = 11.91$, $p = 0.0011$) correlations in the mTBI compared to the sham cohort (Fig. 6C). Following cortical impact, the number of nodes with decreased correlations for the mTBI mice compared to the sham are significantly different at all weeks except week 4 (post-hoc testing with Bonferroni correction). However, for nodes with increased correlations, only week 1 is statistically significant for the mTBI group compared to sham (post-hoc testing with Bonferroni correction). As shown in the examples (Fig. 6A and B), the node count confirms that decreased correlations are the dominant change in the Δ networks following mTBI.

To better visualize the spatial structure of the FC changes following mTBI, we plotted the nodes of each sub-network on the Allen Brain CCF (Fig. 7A, decreased correlations, Fig. 7B, increased correlations), combining the weekly data from the sham and mTBI groups, and computed the density normalized by number of animals and area (in mm^2) for each CCF region. First, these population maps illustrate the sparseness of the Δ network in sham mice versus the greater density of changed nodes throughout the dorsal cerebral cortex in mTBI mice. Second, the maps highlight that the largest disruptions in the network are concentrated in and most often involve ICs in the right motor cortex, the site of the impact. Regions in the contralateral, homotopic cortex also show a high density of change following mTBI. Third, nodes with decreases in correlation strength dominate the weekly Δ networks (Fig. 7A). However, several nodes in the Δ networks increased in correlation strength following mTBI (Fig. 7B), suggestive of a complex reorganization process.

3.3. Functional connectivity of the dorsal cerebral cortex based on LocaNMF

We undertook a second analysis of the changes in FC using LocaNMF (Saxena et al., 2020). In addition to providing an independent evaluation of how mTBI alters cerebral cortical interactions, LocaNMF allows for averaging across mice, as the anatomical segmentation is based on the CCF (see Material and methods). Examination of the average adjacency matrices based on the canonical correlations confirmed the overall stability of the network in sham mice across the entire time span (Fig. 8A), as similarly observed with sICA. Several subnetworks with high correlations among the component subregions, including motor, retrosplenial, and visual regions are evident. Following mTBI, the adjacency matrices show an overall decrease in FC, particularly for these motor, retrosplenial, and visual networks (Fig. 8B). Over the 7 weeks following mTBI, normalized global efficiency significantly decreased ($F(7,5406) = 16.23$, $p < 0.0001$, Fig. 8C), confirming the reduced network integration observed with sICA.

The analysis of network statistics at the nodal level focused on both normalized nodal strength (Fig. 9A) and clustering coefficient (Fig. 9B). For visualization, we plotted the average normalized magnitude of the significant changes relative to baseline for each cortical region, for the sham and mTBI cohorts. For both nodal degree and the clustering coefficient, there are widespread, persistent, bilateral decreases following mTBI (Fig. 9A and B, right columns). The largest amplitude decreases were ipsilateral to the injury site and within the motor, retrosplenial, and somatosensory subnetworks. The sham cohort (Fig. 9A and B, left columns) shows fewer significant changes with a mixture of predominately increases with a few isolated decreases. An important distinction is that in the mTBI cohort, except for two of the smaller atlas regions in nodal strength, a wide-spread consistent decrease in both FC measures occurs over the time course assessed. Also, the changes in the sham cohort occur in later weeks, while for the mTBI cohort, the largest changes in nodal strength and clustering coefficient occur early after CCI. We attribute, the increases in the sham group, at least in part, to the mice becoming increasingly accommodated to the treadmill over time.

3.4. Motor and cognitive characterization of the mTBI model

The network analysis reveals long-lasting changes in FC following mTBI. To examine whether the cortical injury was also associated with impaired motor function, rotarod testing was undertaken in a separate cohort of mTBI (n = 12) and sham (n = 13) mice. We observed no difference in rotarod performance between mTBI or sham animals (F(1,132) = 0.19, p = 0.6602; Fig. 10A), indicating that no overt motor deficit occurred following mTBI.

Barnes maze is a widely used spatial memory task which examines working memory. As no motor deficits were observed in the rotarod task, we expected any deficit in the ability to perform the Barnes maze task following mTBI would be due to impaired cognition (i.e, working memory). Across days, we found no significant difference in the latency to first interaction with the escape hole between sham and mTBI (F (1,88) = 1.94, p = 0.17; n = 6/7, sham/mTBI, Fig. 10B). Additionally, there was no significant difference in the number of poke errors prior to reaching the escape hole between the mTBI and sham groups (F(1,88) = 1.51, p = 0.22; n = 6/7, sham/mTBI). To test whether a cognitive deficit occurred past the short testing period above (3 days), a second group of mice was tested in the Barnes maze 10 days after injury. Despite the longer time following injury, there was no significant difference between mTBI and sham groups in either first latency (F(1,32) = 0.18, p = 0.67; n = 3/3, sham/mTBI) or poke errors (F(1,32) = 0.017, p = 0.90; n = 3/3, sham/mTBI), suggesting there are no cognitive impairments following our mTBI procedure. Taken together, the rotarod and Barnes maze results do not demonstrate deficits in motor function or working memory following mTBI, which is consistent with the sparsity of overt clinical deficits in most humans within 1–3 months following mild TBI (Carroll et al., 2004b).

4. Discussion

We report a new murine model to investigate the effects of mTBI on dorsal cerebral cortical networks using mesoscopic Ca^{2+} imaging of excitatory neurons. We followed cerebral cortical neuronal activity for up to 7 weeks post-mTBI in awake animals to determine the time-course of both acute and subacute changes of cerebral cortical FC. The fundamental findings are that both local and global cerebral cortical network alterations occur following mTBI, as well as brief, transient focal neuroinflammation without appreciable motor or cognitive deficits.

We show that mTBI acutely perturbed the cerebral cortical network observed during baseline, resulting in decreased network similarity. Moreover, the decrease persisted for 7 weeks, suggesting a long-term reorganization of the cortical network. Both sICA and LocaNMF reveal decreased global efficiency following mTBI, indicative of a reduction in functional integration with loss of parallel information transfer (Achard and Bullmore, 2007; Rubinov and Sporns, 2010). The decrease in nodal strength further highlights that mTBI reduces overall functional connectivity. The clustering coefficient is a topological measure of the relationship between any pair of neighbors for each node that provides an assessment of the capacity for information integration within this triad of nodes. While not a direct measure of spatial segregation, the decreases in the clustering coefficient show that mTBI alters the potential for functional specialization by decreasing the number of small, local, functional cortical motifs in the network (Rubinov and Sporns, 2010). Further, the decreases

in nodal strength and clustering coefficient are widespread, involving most of the imaged cortical regions.

The extent of the changes was mapped by the Δ networks, defined by the IC derived nodes with the largest changes in correlation. Compared to the sham animals, the Δ networks in mTBI mice are larger and involve a greater number of nodes. Further, following mTBI, the nodes in the Δ networks are dominated by correlation decreases. While there are changes in nodal density in the Δ networks throughout the cortex, the highest density occurred in somatomotor areas near, as well as contralateral, to the impact site. The LocaNMF results also find that these somatomotor regions exhibit the largest decreases in nodal strength and clustering coefficient.

Although very different mathematically, sICA and LocaNMF provided mutually re-enforcing results. Making no prior assumptions, sICA extracts the cortical regions within each mouse whose neural activity is maximally statistically independent from each other. While a powerful approach to investigate changes within each mouse, sICA poses a challenge to incorporate data across mice. By restricting the localization of activity to the CCF, LocaNMF enables generating cortical networks with identical node locations. This allows averaging FC across mice and achieve a complementary description of the network changes and their cortical locations.

4.1. Comparison to human studies

While some human subject studies describe decreases as well as increases in FC following mTBI (Champagne et al., 2019; Churchill et al., 2017, 2018; Iraji et al., 2016; Johnson et al., 2012; Palacios et al., 2017), persistent disruptions in FC in multiple sensory and cognitive networks are reported in mTBI patients that develop post-concussive syndrome (Stevens et al., 2012; Vakhtin et al., 2013). Moreover, such reduced connectivity persists for up to 4 months (Johnson et al., 2012; Nordin et al., 2016; Shumskaya et al., 2012; Zhou et al., 2012). Taken together, these results suggest that mTBI in patients is commonly characterized by a significant, persistent reduction in connectivity. The decreased connectivity observed in mTBI patients is frequently associated with post- concussive symptoms but not focal motor deficits. Similarly, both sICA and LocaNMF analyses in our study show that the dominant FC change is a decrease. The FC findings, when combined with the mild limited histopathology and behavioral findings, recapitulate several aspects of human disease.

4.2. Wide-field Ca^{2+} imaging provides a novel measure of mTBI on FC

To our knowledge, this is the first report of wide-field Ca^{2+} imaging before and after mTBI, providing new insights into the reduced FC. Imaging based on fMRI or similar approaches are indirect measures of neuronal activity. Our hemodynamic-corrected imaging provides a direct measure of neuronal activity and demonstrates that the reduced FC is due to decreased neuronal activity/function. The Ca^{2+} fluorescence signals detected in the mice (Thy1-GCaMP6f) using our single- photon imaging are primarily from the excitatory neuronal activity in layers II/III (Ma et al., 2016; Waters, 2020; Yizhar et al., 2011). Therefore, the imaging findings are limited to the impact of the mTBI on these neurons. However, imaging cortical layers II/III has the advantage that these layers are the

source of intrahemispheric projections throughout the cortex and interhemispheric projection via callosal axons to equivalent locations in the contralateral cortex (Chovsepian et al., 2017; Zhang et al., 2016), critical projections for FC. The reduction in FC observed is also consistent with the reduction in synchrony in beta band connectivity observed in patients following mTBI (Rier et al., 2021). Therefore, our methodology complements other measures of connectivity by more precisely reflecting neuronal specific changes and their contribution to FC. While our study investigated the effects on FC following mTBI to the motor cortex, it could easily be adapted to examine how mTBI in other brain regions affect FC.

4.3. Comparison to previous rodent models of mTBI

In addition to the chronic wide-field Ca^{2+} imaging, our injury model differs from previous rodent mTBI models using closed head impact (for review see (Bodnar et al., 2019)) as well craniectomy dependent CCI used in the present study (for review see (Siebold et al., 2018)). Few experimental studies have longitudinally characterized changes in cerebral cortical networks at multiple times in the same animal following mTBI beyond one or two time points (Harris et al., 2016; Meningher et al., 2020; Yang et al., 2021). Furthermore, MRI is typically acquired from anesthetized animals. Common anesthesia protocols alter neurovascular coupling (Pan et al., 2015), hemodynamic activity (Ku and Choi, 2012), the extent and magnitude of correlated BOLD response (Bajic et al., 2017), and FC (Mandino et al., 2019; Reimann and Niendorf, 2020).

Several previous studies used moderate/severe TBI that resulted in anatomic lesions and focal neurological deficits (Harris et al., 2016; Yang et al., 2021). As our goal was to study mTBI in awake animals with no/minimal cortical pathology and no hemorrhage, we used a 2 mm, flexible PMMA tip on the impactor as well as very conservative impact parameters (Chen et al., 2014). Compared to previous studies (Siebold et al., 2018), our CCI parameters (1 mm depth, 0.4 m/s) would be classified as “mild”. However, 0.4 m/s is approximately an order of magnitude lower than most previous mTBI studies using CCI. Several studies classified as mild that used higher speeds resulted in greater tissue damage at the injury site as well as parenchymal damage in deeper structures, including the hippocampus, as well as behavior deficits (for review see (Siebold et al., 2018)). The minimal and transient histopathological changes, similarities in the number of ICs extracted and lack of overt behavioral findings in our study are consistent with the impact parameters utilized. In fact, several mTBI studies using more severe impact parameters failed to demonstrate gross motor deficits (Bolte et al., 2020; Sauerbeck et al., 2012) or impairment in spatial memory (Hemerka et al., 2012). Another factor that may have contributed to the lack of a deficit in the Barnes maze is the location of the CCI, which was centered on the right motor cortex. It is possible that if the impact had been delivered more posteriorly, injury to either the cortex over the hippocampus or directly to the retrosplenial cortex, may have resulted in deficits in spatial memory and/or navigation as well as a different distribution of changes in FC.

Previous FC studies in rodents used MRI methodologies. Two rat studies using CCI injury (Harris et al., 2016; Yang et al., 2021) and resting state fMRI, reported increases in connectivity following injury compared to the present results. However, the CCI produced

significant cortical damage in both studies, even in animals classified as having mild injury (Harris et al., 2016). Therefore, these results are consistent with the hyper-connectivity in humans following moderate/severe TBI. A mouse study using diffusion MRI to examine structural connectivity following a closed head impact (Meningher et al., 2020) reported decreased global efficiency and clustering early that returned to normal as well as changes to both hemispheres, as observed here with Ca^{2+} imaging.

5. Conclusions

Our results, when taken together with previous human and experimental studies, highlight that repetitive mTBI can lead to persistent changes in cortical FC. The acute perturbation of cortical connectivity may be due to neural dysfunction during the transient tissue inflammation. In turn, this perturbed network responds to the injury under constraints of maintaining brain functionality. The result is a reorganized cortical network that maintains gross functionality, though in a suboptimal manner. Compensation could play a role in maintaining the behavioral functionality. These findings bear relevance to symptoms experienced by many mTBI patients.

Supplementary Material

Refer to Web version on PubMed Central for supplementary material.

Acknowledgements

We would like to thank Lijuan Zhuo for assistance with animal surgeries. We thank Alexander Cramer at the University of Minnesota University Imaging Center (SCR_20997) for assistance in generating graphics and 3D printing, and the Mouse Behavior Core for behavioral testing. The work was supported in part by NIH R61/R33 NS115089, Minnesota SCI-TBI fund (Grant Contracts: 143722 and 191546), and University of Minnesota's MnDRIVE (Minnesota's Discovery, Research, and Innovation Economy) initiative.

Data availability

Data will be made available on request.

References

Achard S, Bullmore E, 2007. Efficiency and cost of economical brain functional networks. PLoS Comput. Biol. 3, e17. [PubMed: 17274684]

Allen WE, Kauvar IV, Chen MZ, Richman EB, Yang SJ, Chan K, Gradinaru V, Deverman BE, Luo L, Deisseroth K, 2017. Global representations of goal-directed behavior in distinct cell types of mouse neocortex. Neuron 94, 891–907.e6. [PubMed: 28521139]

Bajic D, Craig MM, Mongerson CRL, Borsook D, Becerra L, 2017. Identifying rodent resting-state brain networks with independent component analysis. Front. Neurosci. 11, 685. [PubMed: 29311770]

Biswal B, Yetkin FZ, Haughton VM, Hyde JS, 1995. Functional connectivity in the motor cortex of resting human brain using echo-planar MRI. Magn. Reson. Med. 34, 537–541. [PubMed: 8524021]

Blennow K, Brody DL, Kochanek PM, Levin H, McKee A, Ribbers GM, Yaffe K, Zetterberg H, 2016. Traumatic brain injuries. Nat. Rev. Dis. Prim. 2, 16084. [PubMed: 27853132]

Bodnar CN, Roberts KN, Higgins EK, Bachstetter AD, 2019. A systematic review of closed head injury models of mild traumatic brain injury in mice and rats. J. Neurotrauma 36, 1683–1706. [PubMed: 30661454]

Bolte AC, Dutta AB, Hurt ME, Smirnov I, Kovacs MA, McKee CA, Ennerfelt HE, Shapiro D, Nguyen BH, Frost EL, Lammert CR, Kipnis J, Lukens JR, 2020. Meningeal lymphatic dysfunction exacerbates traumatic brain injury pathogenesis. Nat. Commun. 11, 4524. [PubMed: 32913280]

Burda JE, Bernstein AM, Sofroniew MV, 2016. Astrocyte roles in traumatic brain injury. Exp. Neurol. 275 (Pt 3), 305–315. [PubMed: 25828533]

Caeyenberghs K, Verhelst H, Clemente A, Wilson PH, 2017. Mapping the functional connectome in traumatic brain injury: what can graph metrics tell us? Neuroimage 160, 113–123. [PubMed: 27919750]

Calhoun VD, de Lacy N, 2017. Ten key observations on the analysis of resting-state functional MR imaging data using independent component analysis. Neuroimaging Clin. N. Am. 27, 561–579. [PubMed: 28985929]

Cardin JA, Crair MC, Higley MJ, 2020. Mesoscopic imaging: shining a wide light on large-scale neural dynamics. Neuron 108, 33–43. [PubMed: 33058764]

Cardoso JF, 1999. High-order contrasts for independent component analysis. Neural Comput. 11, 157–192. [PubMed: 9950728]

Carroll LJ, Cassidy JD, Holm L, Kraus J, Coronado VG, WHO collaborating centre task force on mild traumatic brain injury, 2004a. Methodological issues and research recommendations for mild traumatic brain injury: the WHO collaborating Centre task force on mild traumatic brain injury. J. Rehabil. Med. 113–125. [PubMed: 15083875]

Carroll LJ, Cassidy JD, Peloso PM, Borg J, von Holst H, Holm L, Paniak C, Pépin M, WHO collaborating centre task force on mild traumatic brain injury, 2004b. Prognosis for mild traumatic brain injury: results of the WHO collaborating Centre task force on mild traumatic brain injury. J. Rehabil. Med. 84–105. [PubMed: 15083873]

Champagne AA, Coverdale NS, Nashed JY, Fernandez-Ruiz J, Cook DJ, 2019. Resting CMRO2 fluctuations show persistent network hyper-connectivity following exposure to sub-concussive collisions. Neuroimage Clin. 22, 101753. [PubMed: 30884366]

Chen Y, Mao H, Yang KH, Abel T, Meaney DF, 2014. A modified controlled cortical impact technique to model mild traumatic brain injury mechanics in mice. Front. Neurol. 5, 100. [PubMed: 24994996]

Chovsepian A, Empl L, Correa D, Bareyre FM, 2017. Heterotopic transcallosal projections are present throughout the mouse cortex. Front. Cell. Neurosci. 11, 36. [PubMed: 28270750]

Churchill N, Hutchison MG, Leung G, Graham S, Schweizer TA, 2017. Changes in functional connectivity of the brain associated with a history of sport concussion: a preliminary investigation. Brain Inj. 31, 39–48. [PubMed: 27901587]

Churchill NW, Hutchison MG, Graham SJ, Schweizer TA, 2018. Connectomic markers of symptom severity in sport-related concussion: whole-brain analysis of resting-state fMRI. Neuroimage Clin. 18, 518–526. [PubMed: 29560308]

Couto J, Musall S, Sun XR, Khanal A, Gluf S, Saxena S, Kinsella I, Abe T, Cunningham JP, Paninski L, Churchland AK, 2021. Chronic, cortex-wide imaging of specific cell populations during behavior. Nat. Protoc. 16, 3241–3263. [PubMed: 34075229]

Creed JA, DiLeonardi AM, Fox DP, Tessler AR, Raghupathi R, 2011. Concussive brain trauma in the mouse results in acute cognitive deficits and sustained impairment of axonal function. J. Neurotrauma 28, 547–563. [PubMed: 21299360]

Dana H, Chen T-W, Hu A, Shields BC, Guo C, Looger LL, Kim DS, Svoboda K, 2014. Thy1-GCaMP6 transgenic mice for neuronal population imaging in vivo. PLoS One 9, e108697. [PubMed: 25250714]

Fornito A, Zalesky A, Breakspear M, 2015. The connectomics of brain disorders. Nat. Rev. Neurosci. 16, 159–172. [PubMed: 25697159]

Genovese CR, Lazar NA, Nichols T, 2002. Thresholding of statistical maps in functional neuroimaging using the false discovery rate. Neuroimage 15, 870–878. [PubMed: 11906227]

Ghanbari L, Carter RE, Rynes ML, Dominguez J, Chen G, Naik A, Hu J, Sagar MAK, Haltom L, Mossazghi N, Gray MM, West SL, Eliceiri KW, Ebner TJ, Kodandaramaiah SB, 2019. Cortex-wide neural interfacing via transparent polymer skulls. Nat. Commun. 10, 1500. [PubMed: 30940809]

Guizar-Sicairos M, Thurman ST, Fienup JR, 2008. Efficient subpixel image registration algorithms. Opt. Lett. 33, 156–158. [PubMed: 18197224]

Harris NG, Verley DR, Gutman BA, Thompson PM, Yeh HJ, Brown JA, 2016. Disconnection and hyper-connectivity underlie reorganization after TBI: a rodent functional connectomic analysis. Exp. Neurol. 277, 124–138. [PubMed: 26730520]

Hemerka JN, Wu X, Dixon CE, Garman RH, Exo JL, Shellington DK, Blasiole B, Vagni VA, Janesko-Feldman K, Xu M, Wisniewski SR, Bayır H, Jenkins LW, Clark RSB, Tisherman SA, Kochanek PM, 2012. Severe brief pressure-controlled hemorrhagic shock after traumatic brain injury exacerbates functional deficits and long-term neuropathological damage in mice. J. Neurotrauma 29, 2192–2208. [PubMed: 22738159]

Iraji A, Chen H, Wiseman N, Welch RD, O'Neil BJ, Haacke EM, Liu T, Kou Z, 2016. Compensation through functional hyperconnectivity: a longitudinal connectome assessment of mild traumatic brain injury. Neural. Plast. 2016, 4072402. [PubMed: 26819765]

Jacobs EAK, Steinmetz NA, Peters AJ, Carandini M, Harris KD, 2020. Cortical state fluctuations during sensory decision making. Curr. Biol. 30, 4944–4955.e7. [PubMed: 33096037]

Johnson B, Zhang K, Gay M, Horovitz S, Hallett M, Sebastianelli W, Slobounov S, 2012. Alteration of brain default network in subacute phase of injury in concussed individuals: resting-state fMRI study. Neuroimage 59, 511–518. [PubMed: 21846504]

Katz DI, Cohen SI, Alexander MP, 2015. Mild traumatic brain injury. Handb. Clin. Neurol. 127, 131–156. [PubMed: 25702214]

Kristman VL, Borg J, Godbolt AK, Salmi LR, Cancelliere C, Carroll LJ, Holm LW, Nygren-de Boussard C, Hartvigsen J, Abara U, Donovan J, Cassidy JD, 2014. Methodological issues and research recommendations for prognosis after mild traumatic brain injury: results of the international collaboration on mild traumatic brain injury prognosis. Arch. Phys. Med. Rehabil. 95, S265–S277. [PubMed: 24581912]

Ku T, Choi C, 2012. Noninvasive optical measurement of cerebral blood flow in mice using molecular dynamics analysis of indocyanine green. PLoS One 7, e48383. [PubMed: 23119000]

Kumar A, Alvarez-Croda D-M, Stoica BA, Faden AI, Loane DJ, 2016. Microglial/macrophage polarization dynamics following traumatic brain injury. J. Neurotrauma 33, 1732–1750. [PubMed: 26486881]

Lagraoui M, Latoche JR, Cartwright NG, Sukumar G, Dalgard CL, Schaefer BC, 2012. Controlled cortical impact and craniotomy induce strikingly similar profiles of inflammatory gene expression, but with distinct kinetics. Front. Neurol. 3, 155. [PubMed: 23118733]

Lefevre-Dognin C, Cogné M, Perdrieau V, Granger A, Heslot C, Azouvi P, 2021. Definition and epidemiology of mild traumatic brain injury. Neurochirurgie 67, 218–221. [PubMed: 32387427]

Lein ES, Hawrylycz MJ, Ao N, Ayres M, Bensinger A, Bernard A, Boe AF, Boguski MS, Brockway KS, Byrnes EJ, Chen L, Chen L, Chen T-M, Chin MC, Chong J, Crook BE, Czaplinska A, Dang CN, Datta S, Dee NR, Desaki AL, Desta T, Diep E, Dolbeare TA, Donelan MJ, Dong H-W, Dougherty JG, Duncan BJ, Ebbert AJ, Eichele G, Estin LK, Faber C, Facer BA, Fields R, Fischer SR, Fliss TP, Frensley C, Gates SN, Glattfelder KJ, Halverson KR, Hart MR, Hohmann JG, Howell MP, Jeung DP, Johnson RA, Karr PT, Kawal R, Kidney JM, Knapik RH, Kuan CL, Lake JH, Laramee AR, Larsen KD, Lau C, Lemon TA, Liang AJ, Liu Y, Luong LT, Michaels J, Morgan JJ, Morgan RJ, Mortrud MT, Mosqueda NF, Ng LL, Ng R, Orta GJ, Overly CC, Pak TH, Parry SE, Pathak SD, Pearson OC, Puchalski RB, Riley ZL, Rockett HR, Rowland SA, Royall JJ, Ruiz MJ, Sarno NR, Schaffnit K, Shapovalova NV, Sivisay T, Slaughterbeck CR, Smith SC, Smith KA, Smith BI, Sodt AJ, Stewart NN, Stumpf K-R, Sunkin SM, Sutram M, Tam A, Teemer CD, Thaller C, Thompson CL, Varnam LR, Visel A, Whitlock RM, Wohnoutka PE, Wolkey CK, Wong VY, Wood M, Yaylaoglu MB, Young RC, Youngstrom BL, Yuan XF, Zhang B, Zwingman TA, Jones AR, 2007. Genome-wide atlas of gene expression in the adult mouse brain. Nature 445, 168–176. [PubMed: 17151600]

Levin HS, Diaz-Arrastia RR, 2015. Diagnosis, prognosis, and clinical management of mild traumatic brain injury. Lancet Neurol. 14, 506–517. [PubMed: 25801547]

Li F, Lu L, Chen H, Wang P, Chen Y-C, Zhang H, Yin X, 2019. Disrupted brain functional hub and causal connectivity in acute mild traumatic brain injury. Aging 11, 10684–10696. [PubMed: 31754082]

Lin MZ, Schnitzer MJ, 2016. Genetically encoded indicators of neuronal activity. Nat. Neurosci. 19, 1142–1153. [PubMed: 27571193]

Loane DJ, Kumar A, 2016. Microglia in the TBI brain: the good, the bad, and the dysregulated. Exp. Neurol. 275 (Pt 3), 316–327. [PubMed: 26342753]

Loane DJ, Kumar A, Stoica BA, Cabatbat R, Faden AI, 2014. Progressive neurodegeneration after experimental brain trauma: association with chronic microglial activation. J. Neuropathol. Exp. Neurol. 73, 14–29. [PubMed: 24335533]

Ma Y, Shaik MA, Kim SH, Kozberg MG, Thibodeaux DN, Zhao HT, Yu H, Hillman EMC, 2016. Wide-field optical mapping of neural activity and brain haemodynamics: considerations and novel approaches. Philos. Trans. R. Soc. Lond. Ser. B Biol. Sci. 371 10.1098/rstb.2015.0360.

MacDowell CJ, Buschman TJ, 2020. Low-dimensional spatiotemporal dynamics underlie cortex-wide neural activity. Curr. Biol. 30, 2665–2680.e8. [PubMed: 32470366]

Makino H, Ren C, Liu H, Kim AN, Kondapaneni N, Liu X, Kuzum D, Komiyama T, 2017. Transformation of cortex-wide emergent properties during motor learning. Neuron 94, 880–890.e8. [PubMed: 28521138]

Management of Concussion/mTBI Working Group, 2009. VA/DoD clinical practice guideline for Management of Concussion/mild traumatic brain injury. J. Rehabil. Res. Dev. 46. CP1–68. [PubMed: 20108447]

Mandino F, Cerri DH, Garin CM, Straathof M, van Tilborg GAF, Chakravarty MM, Dhenain M, Dijkhuizen RM, Gozzi A, Hess A, Keilholz SD, Lerch JP, Shih Y-YI, Grandjean J, 2019. Animal functional magnetic resonance imaging: trends and path toward standardization. Front. Neuroinform. 13, 78. [PubMed: 32038217]

Marschner L, Schreurs A, Lechat B, Mogensen J, Roebroek A, Ahmed T, Balschun D, 2019. Single mild traumatic brain injury results in transiently impaired spatial long-term memory and altered search strategies. Behav. Brain Res. 365, 222–230. [PubMed: 29499284]

Mathis A, Mamidanna P, Cury KM, Abe T, Murthy VN, Mathis MW, Bethge M, 2018. DeepLabCut: markerless pose estimation of user-defined body parts with deep learning. Nat. Neurosci. 21, 1281–1289. [PubMed: 30127430]

Mayer AR, Mannell MV, Ling J, Gasparovic C, Yeo RA, 2011. Functional connectivity in mild traumatic brain injury. Hum. Brain Mapp. 32, 1825–1835. [PubMed: 21259381]

Meningher I, Bernstein-Eliav M, Rubovitch V, Pick CG, Tavor I, 2020. Alterations in network connectivity after traumatic brain injury in mice. J. Neurotrauma 37, 2169–2179. [PubMed: 32434427]

Musall S, Kaufman MT, Juavinett AL, Gluf S, Churchland AK, 2019. Single-trial neural dynamics are dominated by richly varied movements. Nat. Neurosci. 22, 1677–1686. [PubMed: 31551604]

Nordin LE, Möller MC, Julin P, Bartfai A, Hashim F, Li T-Q, 2016. Post mTBI fatigue is associated with abnormal brain functional connectivity. Sci. Rep. 6, 21183. [PubMed: 26878885]

Palacios EM, Yuh EL, Chang Y-S, Yue JK, Schnyer DM, Okonkwo DO, Valadka AB, Gordon WA, Maas AIR, Vassar M, Manley GT, Mukherjee P, 2017. Resting-state functional connectivity alterations associated with six-month outcomes in mild traumatic brain injury. J. Neurotrauma 34, 1546–1557. [PubMed: 28085565]

Pan W-J, Billings JCW, Grooms JK, Shakil S, Keilholz SD, 2015. Considerations for resting state functional MRI and functional connectivity studies in rodents. Front. Neurosci. 9, 269. [PubMed: 26300718]

Petraglia AL, Dashnaw ML, Turner RC, Bailes JE, 2014. Models of mild traumatic brain injury: translation of physiological and anatomic injury. Neurosurgery 75 (Suppl. 4), S34–S49. [PubMed: 25232883]

Reimann HM, Niendorf T, 2020. The (un)conscious mouse as a model for human brain functions: key principles of anesthesia and their impact on translational neuroimaging. Front. Syst. Neurosci. 14, 8. [PubMed: 32508601]

Ren C, Komiyama T, 2021. Characterizing cortex-wide dynamics with wide-field calcium imaging. J. Neurosci. 41, 4160–4168. [PubMed: 33893217]

Rier L, Zamyadi R, Zhang J, Emami Z, Seedat ZA, Mocanu S, Gascoyne LE, Allen CM, Scadding JW, Furlong PL, Gooding-Williams G, Woolrich MW, Evangelou N, Brookes MJ, Dunkley BT,

2021. Mild traumatic brain injury impairs the coordination of intrinsic and motor-related neural dynamics. Neuroimage Clin. 32, 102841. [PubMed: 34653838]

Rigon A, Duff MC, McAuley E, Kramer AF, Voss MW, 2016. Is traumatic brain injury associated with reduced inter-hemispheric functional connectivity? A study of large-scale resting state networks following traumatic brain injury. J. Neurotrauma 33, 977–989. [PubMed: 25719433]

Rubinov M, Sporns O, 2010. Complex network measures of brain connectivity: uses and interpretations. Neuroimage 52, 1059–1069. [PubMed: 19819337]

Sahonero-Alvarez G, 2017. A comparison of SOBI, FastICA, JADE and infomax algorithms, proceedings of the 8th international multi-conference on complexity, informatics and cybernetics, 2017, pp. 17–22.

Sauerbeck A, Hunter R, Bing G, Sullivan PG, 2012. Traumatic brain injury and trichloroethylene exposure interact and produce functional, histological, and mitochondrial deficits. Exp. Neurol. 234, 85–94. [PubMed: 22201550]

Saxena S, Kinsella I, Musall S, Kim SH, Meszaros J, Thibodeaux DN, Kim C, Cunningham J, Hillman EMC, Churchland A, Paninski L, 2020. Localized semi-nonnegative matrix factorization (LocaNMF) of widefield calcium imaging data. PLoS Comput. Biol. 16, e1007791. [PubMed: 32282806]

Schindelin J, Arganda-Carreras I, Frise E, Kaynig V, Longair M, Pietzsch T, Preibisch S, Rueden C, Saalfeld S, Schmid B, Tinevez J-Y, White DJ, Hartenstein V, Eliceiri K, Tomancak P, Cardona A, 2012. Fiji: an open-source platform for biological-image analysis. Nat. Methods 9, 676–682. [PubMed: 22743772]

Shumskaya E, Andriessen TMJC, Norris DG, Vos PE, 2012. Abnormal whole- brain functional networks in homogeneous acute mild traumatic brain injury. Neurology 79, 175–182. [PubMed: 22744656]

Siebold L, Obenaus A, Goyal R, 2018. Criteria to define mild, moderate, and severe traumatic brain injury in the mouse controlled cortical impact model. Exp. Neurol. 310, 48–57. [PubMed: 30017882]

Spain A, Daumas S, Lifshitz J, Rhodes J, Andrews PJD, Horsburgh K, Fowler JH, 2010. Mild fluid percussion injury in mice produces evolving selective axonal pathology and cognitive deficits relevant to human brain injury. J. Neurotrauma 27, 1429–1438. [PubMed: 20528171]

Stevens MC, Lovejoy D, Kim J, Oakes H, Kureshi I, Witt ST, 2012. Multiple resting state network functional connectivity abnormalities in mild traumatic brain injury. Brain Imag. Behav. 6, 293–318.

Taib T, Leconte C, Van Steenwinckel J, Cho AH, Palmier B, Torsello E, Lai Kuen R, Onyeomah S, Ecomard K, Benedetto C, Coqueran B, Novak A-C, Deou E, Plotkine M, Gressens P, Marchand-Leroux C, Besson VC, 2017. Neuroinflammation, myelin and behavior: temporal patterns following mild traumatic brain injury in mice. PLoS One 12, e0184811. [PubMed: 28910378]

Vakhtin AA, Calhoun VD, Jung RE, Prestopnik JL, Taylor PA, Ford CC, 2013. Changes in intrinsic functional brain networks following blast-induced mild traumatic brain injury. Brain Inj. 27, 1304–1310. [PubMed: 24020442]

Vascak M, Sun J, Baer M, Jacobs KM, Povlishock JT, 2017. Mild traumatic brain injury evokes pyramidal neuron axon initial segment plasticity and diffuse presynaptic inhibitory terminal loss. Front. Cell. Neurosci. 11, 157. [PubMed: 28634442]

Vascak M, Jin X, Jacobs KM, Povlishock JT, 2018. Mild traumatic brain injury induces structural and functional disconnection of local neocortical inhibitory networks via parvalbumin interneuron diffuse axonal injury. Cereb. Cortex 28, 1625–1644. [PubMed: 28334184]

Waters J, 2020. Sources of widefield fluorescence from the brain. Elife 9. 10.7554/eLife.59841.

West SL, Aronson JD, Popa LS, Feller KD, Carter RE, Chiesl WM, Gerhart ML, Shekhar AC, Ghanbari L, Kodandaramaiah SB, Ebner TJ, 2022. Wide-field calcium imaging of dynamic cortical networks during locomotion. Cereb. Cortex 32, 2668–2687. 10.1093/cercor/bhab373. [PubMed: 34689209]

Wu L, Kalish BT, Finander B, Cao T, Jin G, Yahya T, Levy ES, Kukreja B, LaRovere ES, Chung JY, Lo EH, Brown-Whalen A, El Khoury J, Kaplan DL, Whalen MJ, 2022. Repetitive mild closed

head injury in adolescent mice is associated with impaired proteostasis, neuroinflammation, and tauopathy. J. Neurosci. 42, 2418–2432. [PubMed: 35105673]

Xiong Y, Mahmood A, Chopp M, 2013. Animal models of traumatic brain injury. Nat. Rev. Neurosci. 14, 128–142. [PubMed: 23329160]

Xu X, Cowan M, Beraldo F, Schranz A, McCunn P, Geremia N, Brown Z, Patel M, Nygard KL, Khazaee R, Lu L, Liu X, Strong MJ, Dekaban GA, Menon R, Bartha R, Daley M, Mao H, Prado V, Prado MAM, Saksida L, Bussey T, Brown A, 2021. Repetitive mild traumatic brain injury in mice triggers a slowly developing cascade of long-term and persistent behavioral deficits and pathological changes. Acta Neuropathol. Commun. 9, 60. [PubMed: 33823944]

Yang Z, Zhu T, Pompilus M, Fu Y, Zhu J, Arjona K, Arja RD, Grudny MM, Plant HD, Bose P, Wang KK, Febo M, 2021. Compensatory functional connectome changes in a rat model of traumatic brain injury. Brain Commun. 3, fcab244.

Yizhar O, Fenno LE, Davidson TJ, Mogri M, Deisseroth K, 2011. Optogenetics in neural systems. Neuron 71, 9–34. [PubMed: 21745635]

York EM, LeDue JM, Bernier L-P, MacVicar BA, 2018. 3DMorph automatic analysis of microglial morphology in three dimensions from ex vivo and in vivo imaging. eNeuro 5. 10.1523/ENEURO.0266-18.2018.

Zhang S, Xu M, Chang W-C, Ma C, Hoang Do JP, Jeong D, Lei T, Fan JL, Dan Y, 2016. Organization of long-range inputs and outputs of frontal cortex for top-down control. Nat. Neurosci. 19, 1733–1742. [PubMed: 27749828]

Zhou Y, Milham MP, Lui YW, Miles L, Reaume J, Sodickson DK, Grossman RI, Ge Y, 2012. Default-mode network disruption in mild traumatic brain injury. Radiology 265, 882–892. [PubMed: 23175546]

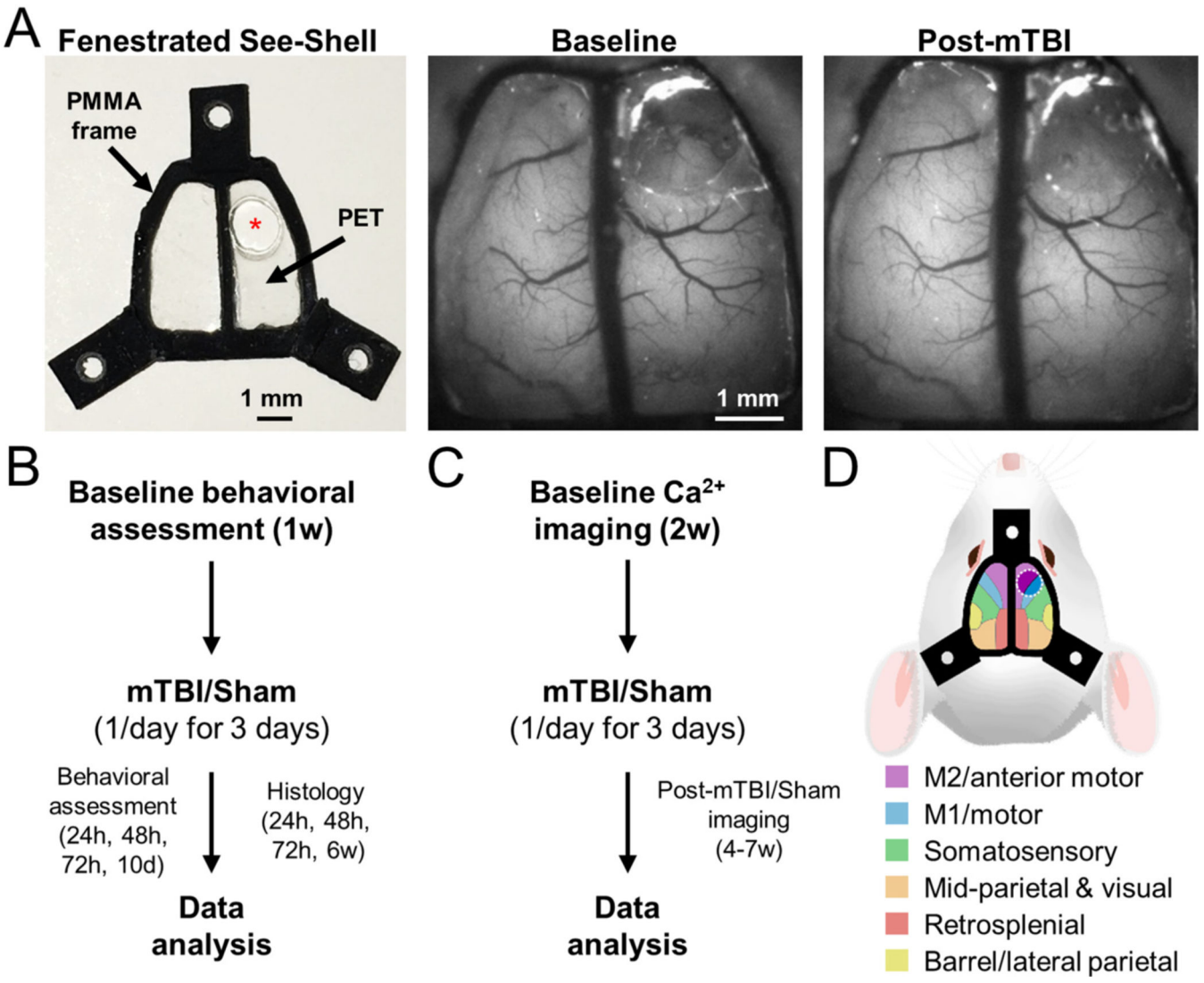

Fig. 1. Implant and experimental design.

A. (*left*) Image of the fenestrated See-Shell (* indicates opening in the PET). (*middle*) Baseline fluorescence image from a Thy1-GCaMP6f mouse 2 weeks after implantation of the fenestrated See-Shell. The PET opening is covered with a thin layer of a silicon polymer (Kwik-Sil). (*right*) Image from the same mouse 2 days post-mTBI. **B & C.** Experimental design of the behavioral and histological assessments (***B***) and the Ca^{2+} imaging (***C***). **D.** Illustration of the cortical regions (color coded to match legend) imaged through the fenestrated See-Shell. White-dashed circle denotes the opening in the PET.

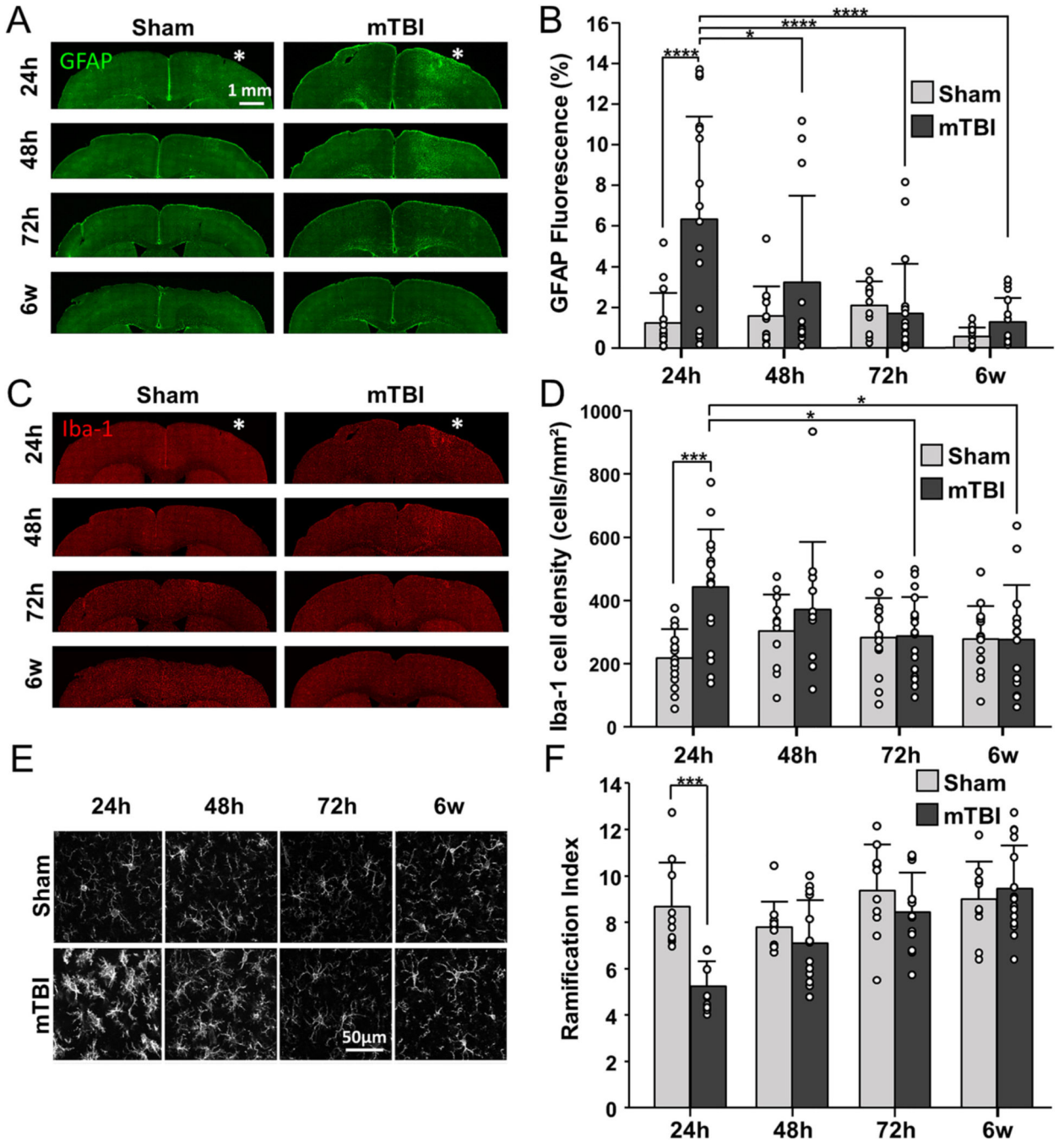

Fig. 2. Changes in GFAP and Iba-1 expression following mTBI.

A & C. Example immunostaining for GFAP (***A***) and Iba-1 (***C***) over time for sham (*left*) and mTBI (*right*) animals. * denotes ipsilateral site of the PET opening. **B & D**. Quantification of GFAP expression (***B***) and Iba-1 cell density (***D***). mTBI induced significantly higher global GFAP expression at 24 h compared to sham animals (n = 5/6, sham/mTBI; p < 0.0001), while it decreased significantly from 24 h to 48 h, 72 h, and 6w following mTBI (n = 6; p = 0.0195, p < 0.0001, p < 0.0001, respectively). Significantly higher Iba-1 cell density occurred at 24 h in mTBI compared to sham (n = 5/6, sham/mTBI; p < 0.0001), and

decreased significantly from 24 h to 72 h and 6w for mTBI animals (n = 6; $p = 0.0121$, p = 0.0121, respectively). **E**. Confocal images of Iba-1 showing microglia activation at 24 h in mTBI (*bottom*) compared to sham animals (*top*). **F.** Microglial ramification was significantly lower in mTBI animals at 24 h compared to sham (n = 5/5 sham/mTBI, $p < 0.05$). Open circles in all plots are individual data points. *, ***, **** denotes p < 0.05, 0.001, and 0.0001, respectively.

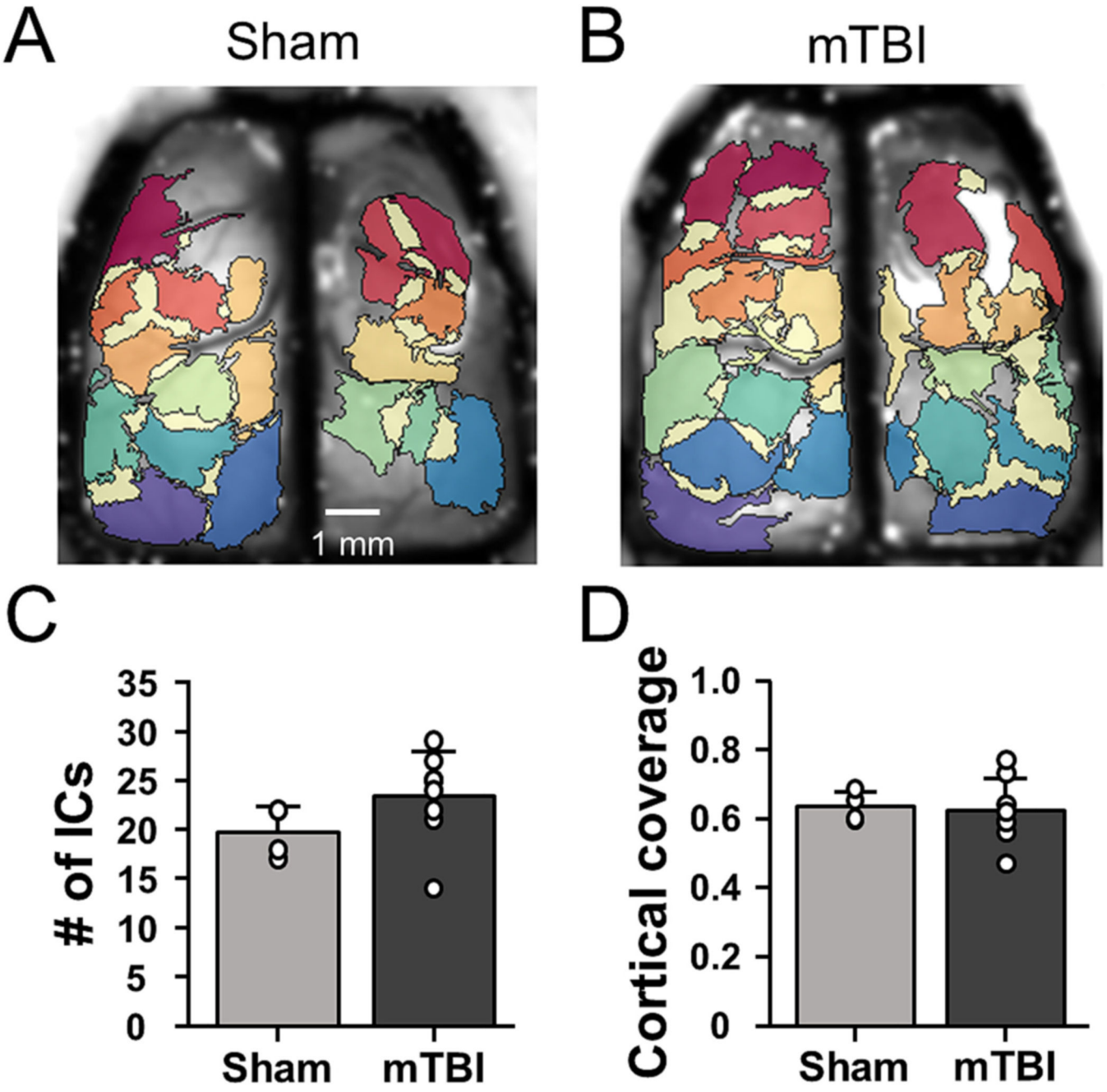

Fig. 3. Functional cortical segmentation using sICA.

A & B, Examples of cortical functional segmentation into ICs obtained over the entire optical recording data set, for a sham (**A**) and mTBI (**B**) mouse. **C**, Number of ICs did not differ between the sham and mTBI groups ($t = -1.450$, $p = 0.178$, Student t-test). **D,** Percent coverage by the ICs of the dorsal cortex, which did not differ between the sham and mTBI groups ($t = 0.237$, $p = 0.817$, Student t-test).

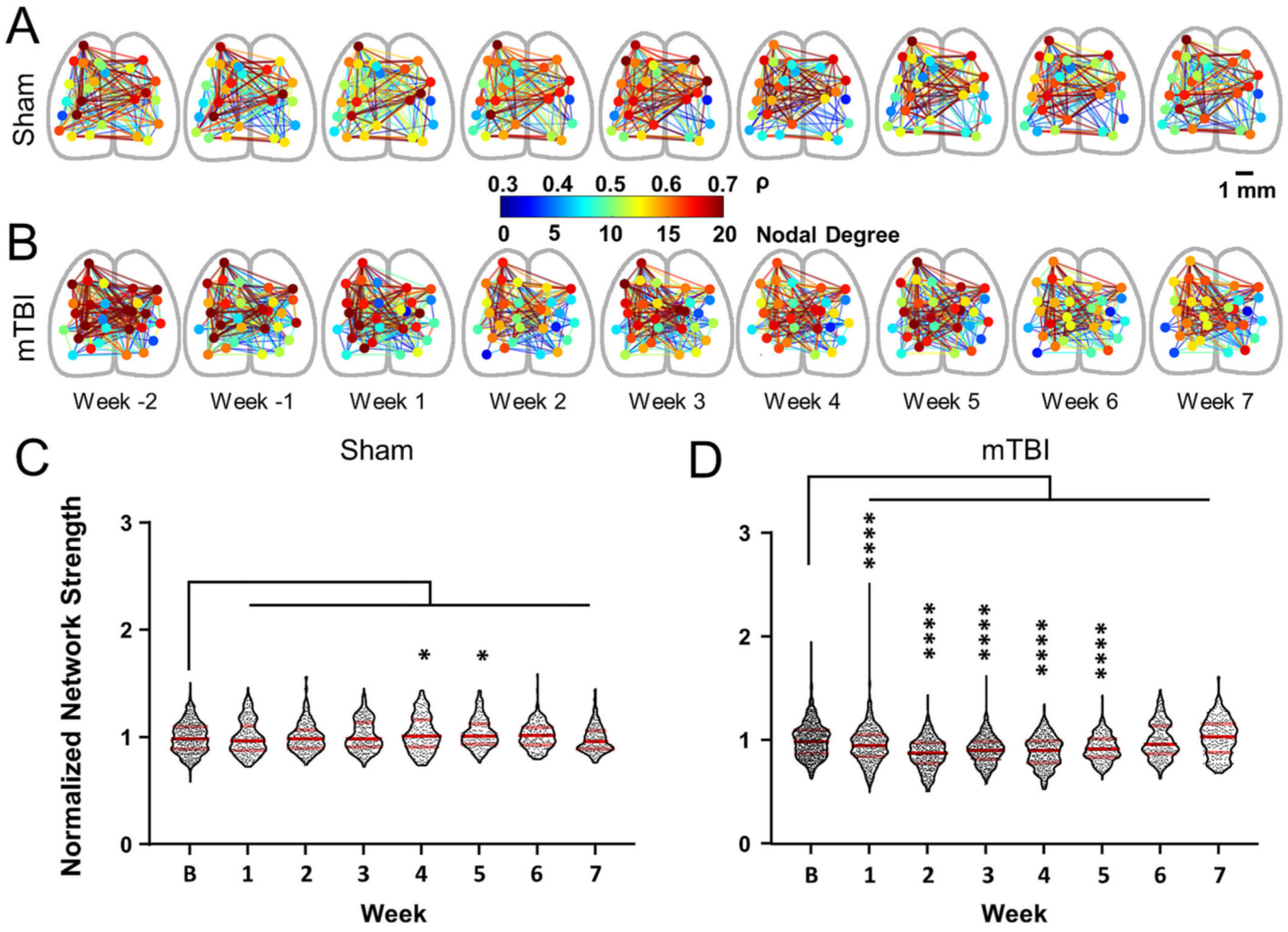

Fig. 4. Functional connectivity networks.

A & B. Examples of FC at each week in a sham (**A**) and a mTBI (**B**) animal. Node positions are the center of mass of ICs, plotted on a simplified outline of the dorsal cortex. The connections shown include only correlation coefficients (ρ) > 0.3. Nodes are color-coded to nodal degree. Edges are color-coded to ρ. **C & D.** Average correlation strength for all connections, normalized to the average baseline strength for sham (**C**) and (**D**) mTBI groups. All comparisons are relative to the group baseline (Week B). * and **** denote $p < 0.05$ and 0.0001, respectively. Violin plots show the individual points for each minute for all animals, with the median and quartiles denoted by the dark and light red bars, respectively. (For interpretation of the references to color in this figure legend, the reader is referred to the web version of this article.)

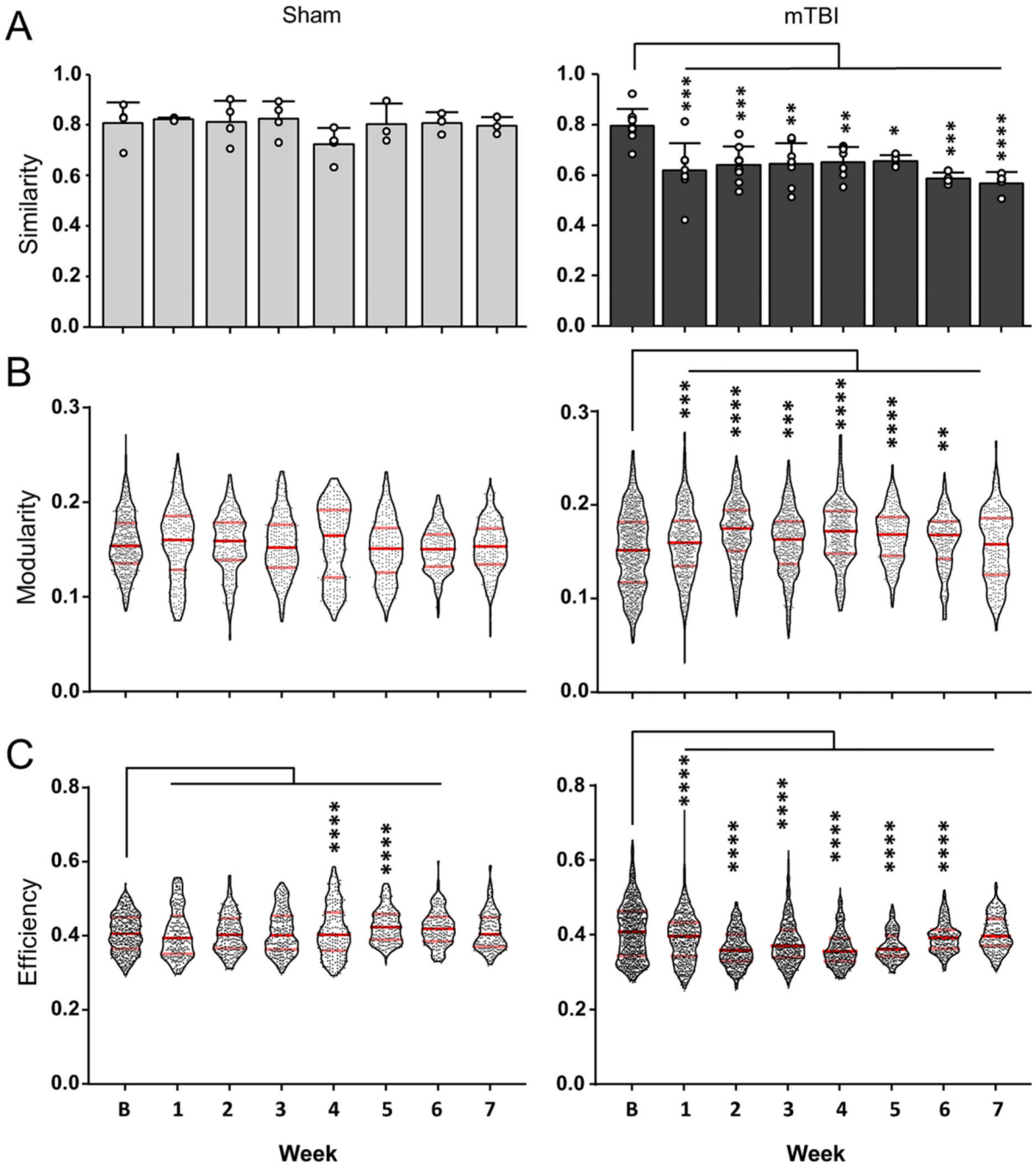

Fig. 5. Functional connectivity network quantitative descriptors from sICA.

A. Group summary plots of the Similarity Index. Individual points are the weekly average for each animal. **B.** Group summary plots of the full network global modularity. **C.** Group summary plots of the full network global efficiency. All comparisons are relative to the group baseline (Week B). *, **, ***, **** denote $p < 0.05$, 0.01, 0.001, and 0.0001, respectively. Violin plots show the individual points for each minute for all animals, with the median and quartiles denoted by the dark and light red bars, respectively. (For interpretation

of the references to color in this figure legend, the reader is referred to the web version of this article.)

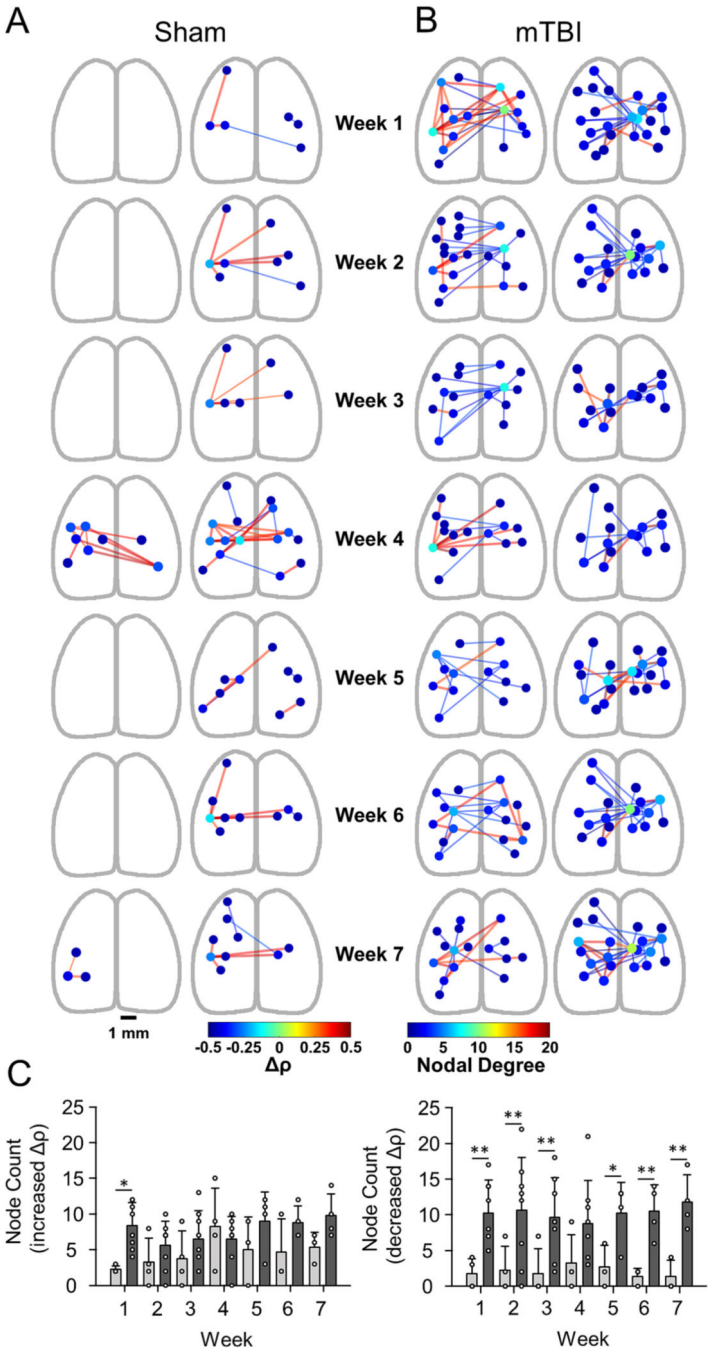

Fig. 6. Δ networks. A & B.

Example of the Δ networks at each week in two sham animals (***A***) and two mTBI animals (***B***). Nodes are color-coded to nodal degree. Edges are color-coded to change in correlation coefficient (Δρ, blue = decrease; red = increase). **C.** Quantification of the number of nodes in the Δ networks that have either an increase (left) or decrease (right) change in correlation coefficient. * and ** denote $p < 0.001$ and 0.0001, respectively. Individual points are the weekly average for each animal.

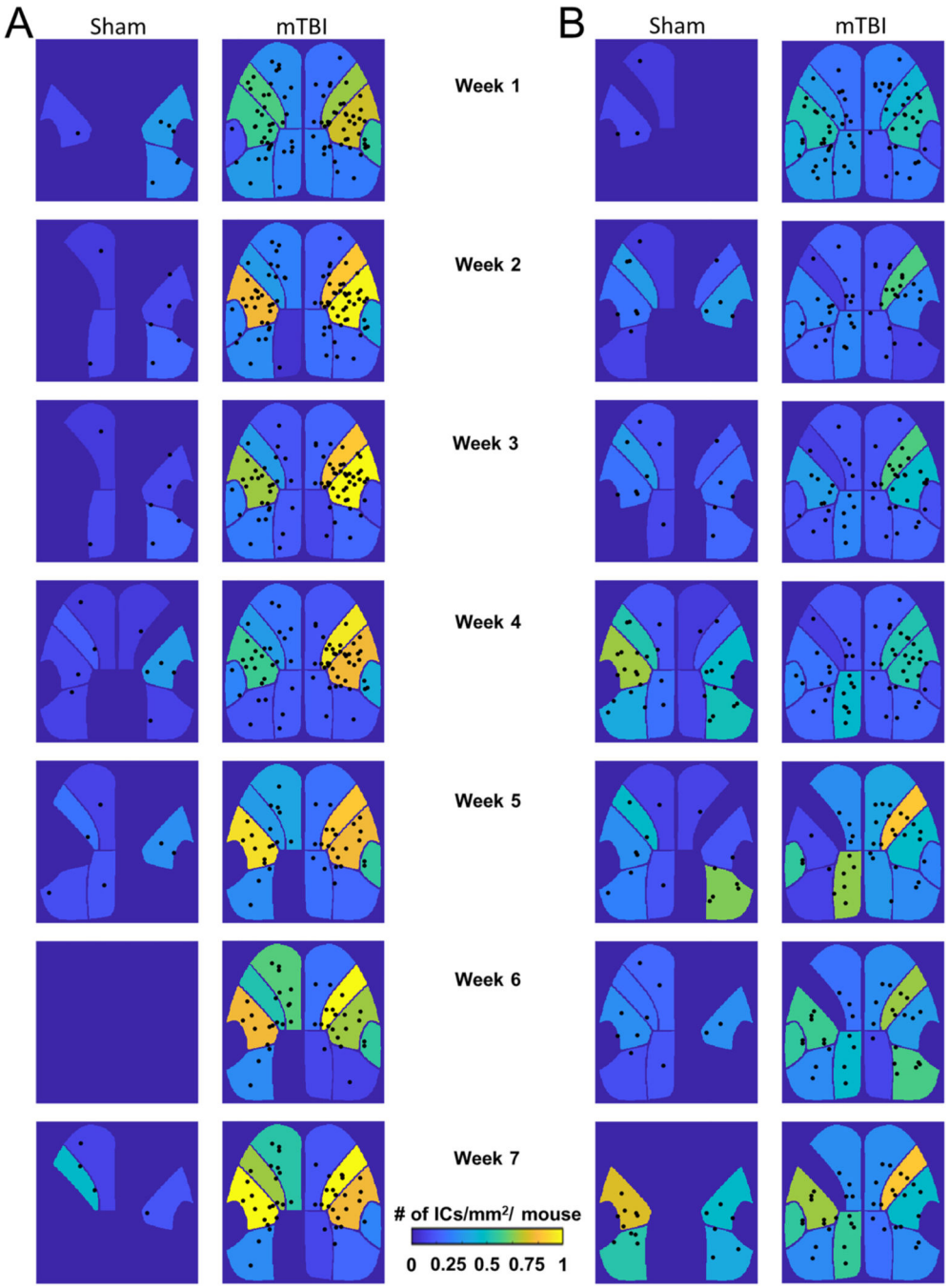

Fig. 7. Effects of mTBI on IC density. A & B.

Center of mass of ICs that showed significant decreases (***A***) or increases (***B***) following sham (*left*) or mTBI (*right*), plotted on a canonical segmentation of the cerebral cortex (Allen Brain Atlas). Each cortical region (see Fig. 1D for labels) is color-coded to the density of ICs normalized to the number of mice in each group and week.

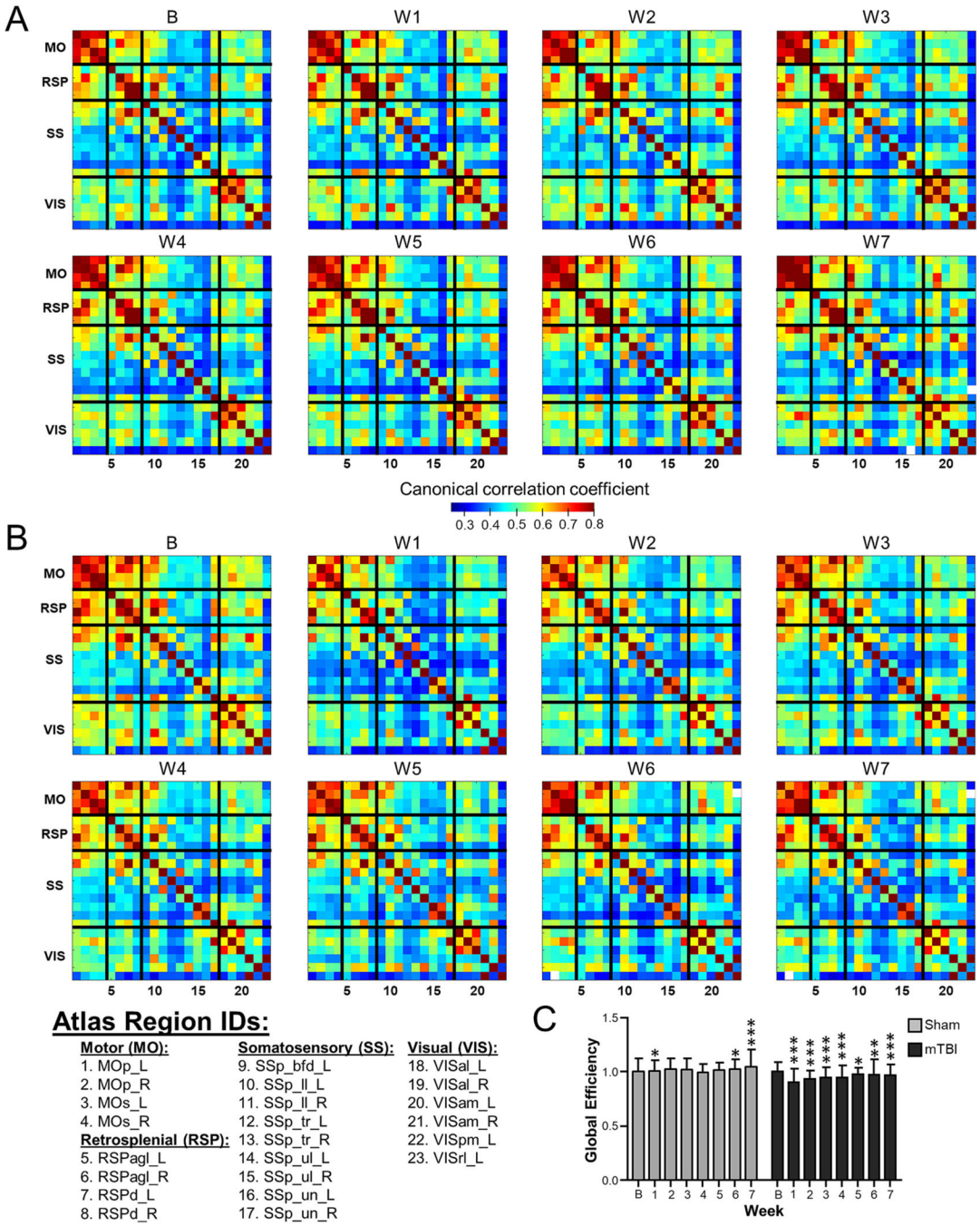

Fig. 8. Large-scale decreases in FC following mTBI revealed by LocaNMF. A & B.

Canonical correlation matrices from all sham (***A***) and mTBI (***B***) mice over time across the Allen Brain Atlas regions in all mice. Regions are grouped into generic functional areas which are separated by black lines. Atlas region abbreviations are provided (for full names, see Material and methods). Correlations between regions were evaluated by false discovery rate with white pixels being not significant. **C.** Normalized global efficiency calculated from the weighted correlation matrices from each 1-min imaging time bin. *, **, *** denotes $p < 0.05$, 0.01 and 0.0001, respectively. Individual data points are not shown for visual clarity.

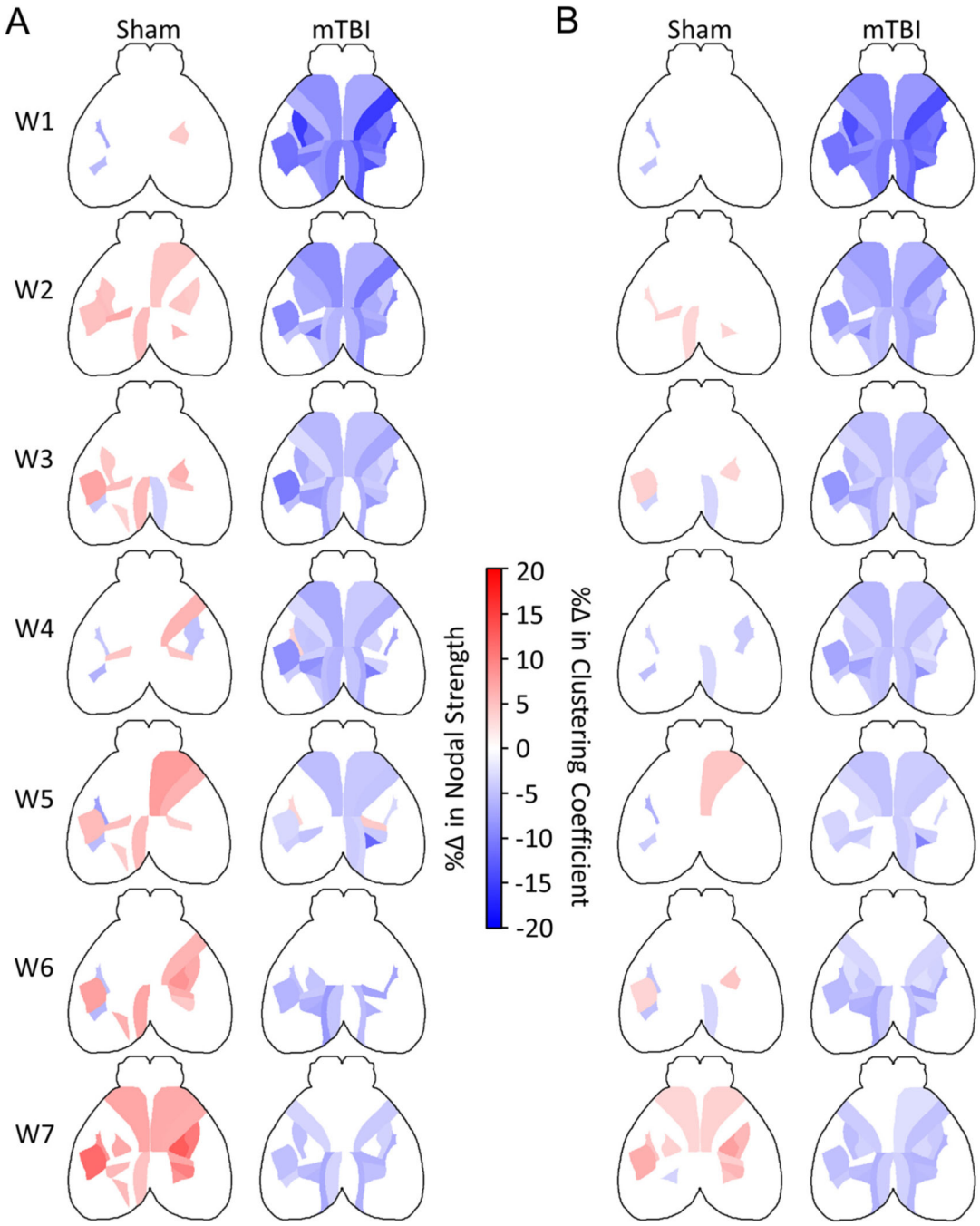

Fig. 9. Significant decreases in functional connectivity metrics following mTBI revealed by LocaNMF. A.

Changes in normalized nodal strength from sham (*left*) and mTBI (*right*) color-coded to magnitude of the change for each atlas region that was significantly different from baseline. **B.** Same as in (***A***) but for the normalized clustering coefficient. Only atlas regions that remained significant following Bonferroni's post-hoc correction ($p < 0.05$) are shown.

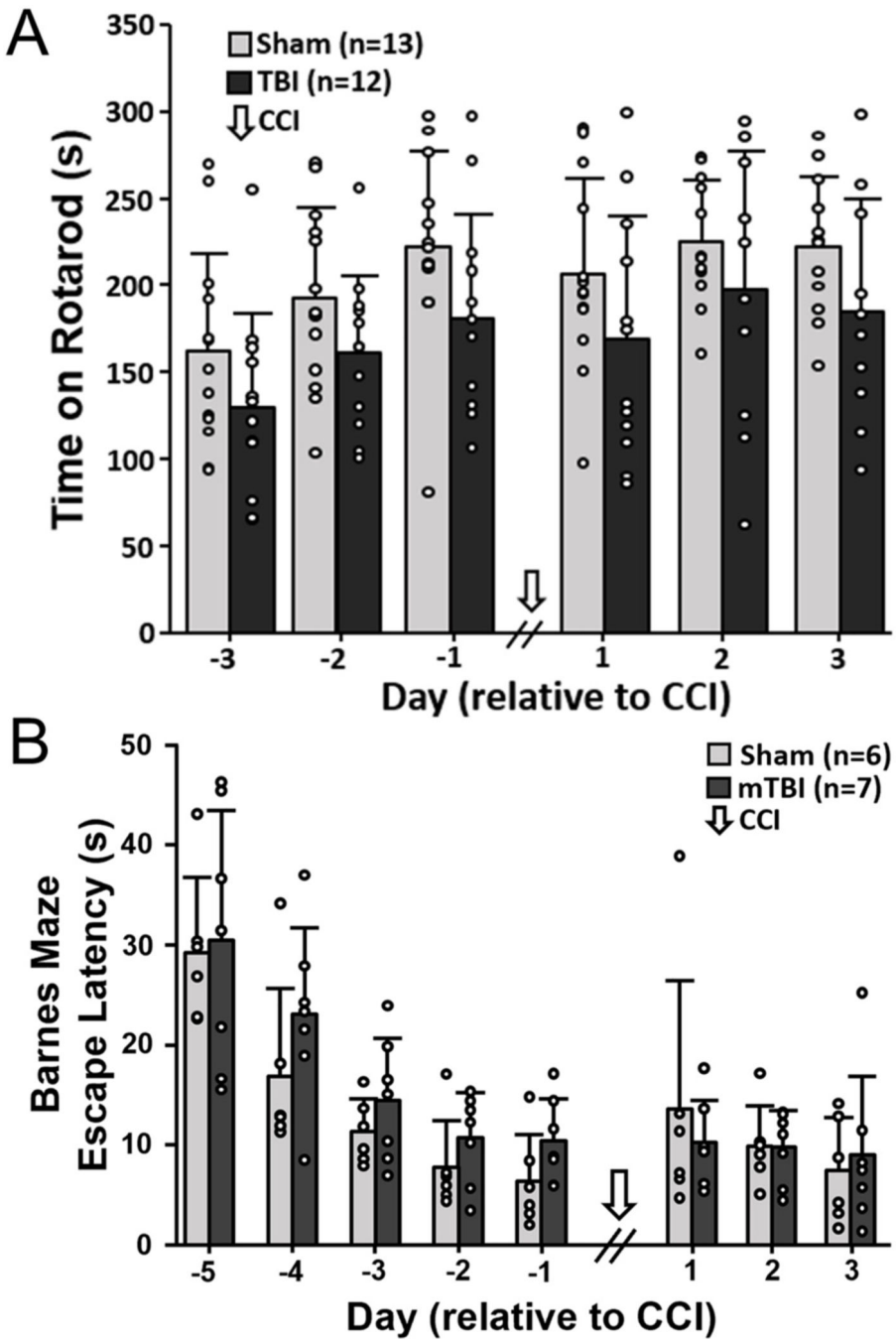

Fig. 10. Motor and cognitive function are unaffected by mTBI. A.
Rotarod performance between sham and mTBI animals. Data points presented as the average of 4 daily trials per animal, normalized to Day − 1. **B.** Barnes maze escape latency between sham and mTBI animals. Latencies were averaged for the 4 daily trials per mouse, except probe days (Days − 1 and 3) where only 1 trial was performed. White arrow denotes the time of CCI.